AUTONOMOUS NAVIGATION OF RELATIVISTIC SPACECRAFT: THEORY AND APPLICATIONS

A Dissertation

Presented to the Faculty of the Graduate School

of Cornell University

In Partial Fulfillment of the Requirements for the Degree of

Doctor of Philosophy

by

Doğa Yücalan

August 2022

AUTONOMOUS NAVIGATION OF RELATIVISTIC SPACECRAFT:
THEORY AND APPLICATIONS

Doğa Yücalan, Ph. D.
Cornell University 2022

This dissertation introduces a relativistic autonomous observation model that takes special relativistic mechanics as a baseline and is more general than Einstein's observation model. Next, it presents two autonomous navigation methods that build on the relativistic autonomous observation model. These methods utilize an onboard star catalog and astrometry and spectrometry sensors and estimate astrometric and spectrometric quantities in addition to spacecraft position and velocity. A case study investigates the performance of both navigation methods in the context of technological details of a near-term mission, including certain sources of noise and disturbance in the interstellar medium. Results of the case study suggest that these methods are suitable for any spacecraft for which relativistic effects are detectable onboard. Moreover, the methods' success in estimating astrometric and spectrometric quantities may enable means of updating the star-catalog during the mission and may improve the accuracy of our current star catalogs. Finally, the dissertation presents a technology-push mission concept for an interstellar dark matter explorer mission that the two navigation methods enable. This mission concept employs well-understood and space-demonstrated technology of several heritage spacecraft. It proposes a new idea to detect deviations in the dark matter distribution within the solar system and looks promising even in

this early development stage. Overall, this dissertation represents a foundational step in the development of interstellar navigation technology and interstellar dark matter exploration missions.

BIOGRAPHICAL SKETCH

Doğa Yücalan was born on a small planet in the Milky Way galaxy to loving and supportive parents. Doğa learned how to read at three years old and how to write at four. Doğa started authoring poems about everyday life and loving math, science, space, cats, the Sun, sheep, and willow trees as early as five. This love eventually left Doğa wanting to learn everything about everything, and they excelled as a student in K-12 in all classes but history and religion.

Still, Doğa wanted to learn increasingly. Doğa graduated from Middle East Technical University, in Ankara, Turkey, with a Bachelor of Science in Electrical and Electronics Engineering and a double major in Physics in 2016. At this point, Doğa had learned a lot, but it still did not feel enough. So, Doğa came to Cornell University, in Ithaca, NY, to become a Doctor of Aerospace Engineering with minors in Astronomy and Theoretical Physics.

Now, Doğa has learned a little too much, and would like to give back to the universe by teaching people how to learn what they want to learn. After defending their dissertation in July 2022, Doğa will become an Assistant Professor of Teaching in the Department of Engineering Education at the University of Buffalo in Buffalo, NY.

Dedicated to the universe, thank you for *everything*.

ACKNOWLEDGEMENTS

For his continual patience, inspiration, support, and kindness, I would like to endlessly thank my adviser, Mason Peck. For supporting my research financially, I would like to thank Zonta International. For helping me stay in love with math and physics, I would like to thank my committee members, Dmitry Savransky and Thomas Hartman. For their honesty, cheerfulness, and support in my doctoral journey, I would like to thank all past and present members of my lab, Space Systems Design Studio, as well as the members of Space Imaging and Optical Systems Lab with whom I shared my office.

For inspiring me to be a better teacher and believing that I can, and for giving me many opportunities to practice teaching while being wonderfully kind and supportive, I would like to thank Celia Evans, Hadas Ritz, Ben Finio, Hadas Kress-Gazit, Derina Samuel, and the rest of my teaching community at Cornell. For helping me navigate the academia while staying kind to myself and others, and for making me feel special in this cruel jumble, I would like to thank Amanda Baird, Marcia Sawyer, Katrina Overton, Don Parker, Patti Wojcik, Colleen McLinn, and Sara Xayarath-Hernandez.

For being perfect friends and wonderful and funny human beings, I would like to thank Kasey Laurent, Dean Keithly, Lena Thiry, Reece Kearney, and Josh Solberg. For being the “life” of my work-life balance, I would like to thank Michael Suguitan, Zoe Pollard, Gabriel Soto, Jacob Shapiro, Emily Rosello Mercurio, Kristine Lai, Patrícia Alves-Oliveira, Ameli Martha, Adam Pacheck, Hyunji Kim, Brian Wang, Cameron Aubin, Jeanie Aird, Akane Wakai, Emily Bernal, Zoe Scopa, Haley Miller, and all the other friends I made in Ithaca.

For making it ridiculously hard going back to just dancing “regular salsa,” I would like to thank Michael Ristorucci, Luis Lezcano, Nicole Beltran, Juan Gabriel Berrio, Alexa Podolsky, Ruju Dani, Kunal Pattanayak, Oleg Gorobtsov, Robert Okun, Carlos Brizuela, Kanat Bolazar, Zain Lugay, Alice Li, and all my other salsa rueda friends. For telling me to come back because they miss me and also not to come back because everything sucks there, I would like to thank all my friends in Turkey. I miss you so much!!

For being perpetually ready to jump on a plane, I would like to thank my mom, Özgül Yücalan. For loving, raising, and supporting me, I would like to thank my dad, Turgut Yücalan, my aunt, İnci Melek Çağlar, my stepdad, Atalay Girgin, my stepsister, Deniz Girgin, my grandparents, Fatma Koçer, Mehmet Yücalan, and Nahide Yücalan, and my friends, Leyla İpek and Tekgül Arı. For teaching me to think critically and care unfathomably, I would like to thank my teachers, Semra Çetinkaya and Yücel Dündar.

For being the piece of my heart that I miss the most, I would like to thank my best friend, Evin Su Bozdağ. For being the two pieces of my heart that bind me to this planet and help me breathe, I would like to thank my best friend, Ajla Lejlić, and my godson, Vanja.

For holding my hand, keeping me sane, helping me grow, making me laugh, finding me funny, and loving me forever, I would like to thank my partner and best friend, Arnaldo Rodríguez-González.

Finally, for simply existing, I would like to thank Doğa Yücalan. I love you and I am proud of you, and I hope you will never have to do this again.

TABLE OF CONTENTS

LIST OF FIGURES

LIST OF TABLES

LIST OF ABBREVIATIONS

AU	astronomical unit
DLR	Deutsches Zentrum für Luft- und Raumfahrt (German Aerospace Center)
DSN	Deep Space Network
EGG	Electrostatic Gravity Gradiometer
ESA	European Space Agency
ESO	European Southern Observatory
GOCE	Gravity Field and Steady-State Ocean Circulation Explorer
GPS	Global Positioning System
GRACE	Gravity Recovery and Climate Experiment
GRACE-FO	Gravity Recovery and Climate Experiment Follow-On
GRAIL	Gravity Recovery and Interior Laboratory
ISM	interstellar medium
LEO	low Earth orbit
LH2	liquid Hydrogen
LOX	liquid Oxygen
MATLAB	Matrix Laboratory
MMH	monomethyl hydrazine
NASA	The National Aeronautics and Space Administration
NICER	Neutron-Star Interior Composition Explorer
N2O4	Nitrogen tetroxide

RTG	radioisotope thermoelectric generator
SI	Système international d'unités (International System of Units)
USD	United States dollar
VLBI	Very long baseline interferometry
XNAV	X-ray pulsar-based navigation and timing

CHAPTER 1

INTRODUCTION

Interstellar space exploration missions

Over 60 years of space exploration missions have mostly been confined to our solar system. So far, only three NASA spacecraft, all launched in the 1970s, have departed the heliosphere and have reached interstellar space [1]. Among the three, only Voyagers 1 and 2 were still transmitting science data back to Earth while doing so over 35 years after they were launched [2]. Both spacecraft are still functioning as of June 2022, at 156 and 130 astronomical units (AU) from the Sun, respectively [3].

Our current understanding of interstellar space comes from several sources. The Voyagers are still transmitting *in-situ* data on the magnetic field, low- and high-energy charged particles, radio emissions, and hydrogen distribution in the outer regions of the solar system [4]. Because of them, we know that interstellar space begins at approximately 120 AU from the Sun. Other sources of information include telescopes [5–7] and particle detectors [8] that are on or near the Earth, analyzing photons and particles that carry information about their origins. What we currently lack is more *in-situ* data from interstellar space, particularly related to less-understood physical phenomena or objects such as dark matter.

The idea of dark matter first emerged in the early 20th century due to an inconsistency between measurements of velocities of stars in galaxies and

galaxies in galaxy clusters: those far away from the center were moving much faster than our understanding of gravity predicts. However, this discrepancy did not become a central concern until the 1970s, when there was enough evidence to support this claim [9,10]. So far, all evidence of dark matter's existence and all information regarding its nature comes from astrometric, spectrometric, and photometric observations of celestial bodies or cosmic radiation, and gravitational lensing measurements [10–13]. Much of this evidence can be summarized with a few words: dark matter is massive, it does not interact electromagnetically, and it represents approximately 85% of all the matter in the universe [14].

Currently, there are many terrestrial or near-Earth efforts to search for additional information about dark matter using different techniques. These techniques look for dark matter directly or indirectly. Direct methods look for interactions of ordinary matter with dark matter, such as dark matter particles' elastic scattering on atomic nuclei [15]. Meanwhile, indirect methods try to find products of dark matter due to its interaction with itself or ordinary matter. Indirect methods either try detecting these products directly [16] or look for discrepancies in the results of collider experiments [8]. So far, none of these methods has yielded conclusive results. Not being able to understand such a fundamental part of our universe, especially one that has strong connections to its current structure and evolution, is a priority for the science community, even included in the 2020 Decadal Survey on Astronomy and Astrophysics [17].

The way to understand dark matter may lie in Einstein's equivalence principle: physics in an accelerating frame is locally indistinguishable from physics in a gravitational field [18]. Recent simulations [19] and observations [12] suggest that the Milky Way may have an uneven distribution of dark matter. A spacecraft designed to detect acceleration could sense the gravitational effects of nearby dark matter. However, until now, no solar system exploration mission that explicitly measures acceleration sensed these effects. The most likely reason of this lack of evidence is that the gravitational acceleration due to the Sun and other massive bodies in the solar system is much greater than that of dark matter. Another likely reason is that no spacecraft was specifically looking for these effects [20]. Therefore, a space exploration mission aiming to detect dark matter needs to employ spacecraft located far enough away from ordinary matter's gravitational interactions within the solar system.

Sending a spacecraft far from the solar system's gravitational influence and returning science data within a human lifetime requires spacecraft to travel at speeds much greater than what today's interstellar spacecraft achieve. To illustrate this fact, consider a mission to long-period comets with aphelia at about 50,000 AU [21]—a mission consistent with the science priorities in the 2022 Planetary Science and Astrobiology Decadal Survey [22]. The greatest speed a spacecraft can attain with our current technological capabilities is 40 AU/yr, which is the speed Parker Solar Probe will reach in 2024 [23]. Even at this speed, reaching 50,000 AU would take 1,250 years.

There are many technological obstacles that must be overcome before spacecraft can travel fast enough to realize missions to 50,000 AU and beyond. Most of these obstacles are related to the state of the art in propulsion and energy storage technology [24]. Multiple research groups are interested in solving these challenges [25–27], including Breakthrough Initiatives—a multi-million-dollar program searching for extraterrestrial life. Their Breakthrough Starshot project [28] is looking to send 2.5-gram chip satellites [29,30] to Proxima Centauri at 20% of the speed of light, accelerated with beamed power propulsion [26,31]. A more near-term example of a 10-kg spacecraft with the same propulsion design reaches only to 2% of the speed of light at the edge of the solar system [31]. Future propulsion techniques such as this one could enable a mission that measures the dark matter distribution in the outer regions of the solar system in the near future.

Deep space spacecraft navigation and the state of the art

Navigation of spacecraft refers to the estimation of, at a minimum, the position and velocity of the spacecraft in some useful frame of reference. State-of-the-art navigation algorithms for deep space missions (farther than the Moon) are either Earth-based or autonomous. Earth-based algorithms, as the name suggests, use technology located on Earth in tandem with those on spacecraft to estimate spacecraft's location. Autonomous algorithms, in contrast, navigate using only the sensors onboard the spacecraft.

State-of-the-art Earth-based algorithms for deep space navigation employ radiometric measurements and NASA's Deep Space Network (DSN). Examples of these techniques include round-trip time-of-flight and Doppler-shift measurements of signals between Earth and the spacecraft. Another example is Very Long Baseline Interferometry (VLBI), which utilizes radiation emitted by extragalactic astronomical objects and locates the spacecraft by comparing the signals as received by the spacecraft and the DSN. One final example is Delta-Differential One-Way Ranging, which calculates the time difference between arrival times of two ranging signals departing two distinct antennas. This time difference is filtered to provide a relative distance [32]. These techniques are flight-proven, and therefore most space exploration missions today utilize them.

Only two deep space autonomous navigation algorithms are flight proven. The first is AutoNav, used in many deep space comet and asteroid, flyby and encounter missions by NASA. This algorithm tracks nearby objects using optical sensors to navigate [33,34]. The second is XNAV, designed as a deep-space-suitable navigation algorithm that was demonstrated as a part of NASA's NICER mission on the International Space Station [35,36]. The XNAV algorithm uses X-ray emissions from pulsars to locate the spacecraft. In addition to these demonstrated technologies, there are several other autonomous navigation algorithms based on Newtonian mechanics in development [37–43]. These algorithms may be suitable for deep-space use and may become flight-proven in the near future.

Inadequacies of the state of the art for interstellar missions

None of the navigation technologies summarized above are adequate for a future interstellar space exploration mission for two reasons. First, any method with Earth in the loop gets affected by geometric dilution of precision [44] and time delay. These factors compromise accuracy to the point where navigation performance is inferior beyond the heliopause. Second, treating relativistic effects as perturbations to Newtonian physical laws introduces calculation errors that significantly worsen as the spacecraft speed increases.

In addition to these challenges, the interstellar medium (ISM) may alter the trajectory of spacecraft unexpectedly. Using an open-loop navigation method is inadequate in interstellar space while it stays as an uncertain environment. To justify these claims, consider again the mission example to 50,000 AU. For the purpose of this example, the spacecraft travels at 2% of the speed of light to its destination, similar to the 10-kg spacecraft in [31].

Why Earth-based navigation does not work for this mission: From 50,000 AU, the Earth subtends roughly 1.7 nrad (0.35 mas). The state-of-the-art astrometry mission Gaia's angular resolution is in μas range [45], and the state of the art in spacecraft pointing is in the μas range [46]. Then, a spacecraft could successfully resolve Earth and point at it. However, the 50,000 AU distance would delay the information sent from the Earth to the spacecraft by over nine months. Such a delay would prevent Earth-based closed-loop navigation.

Why autonomous navigation based on Newtonian mechanics does not work for this mission: If the spacecraft is traveling at 2% of the speed of light, the relativistic time dilation results in about 17 s/day difference in travel time as reckoned on the spacecraft. If the speed is increased by a factor of 10, this time difference increases by a factor of 100. In comparison, the error experienced by GPS satellites due to effects of special and general relativity is around 38 μs/day [47]. These effects would cause a Newtonian algorithm to be inaccurate.

Why an open-loop method does not work for this mission: 2% of the speed of light is high enough for the ISM particles to collide with the spacecraft, lower its velocity, and raise its potential [48]. As a result, the charged spacecraft may slow down and deviate from its trajectory due to the interstellar magnetic field, which has some unknown strength and orientation. In this mission example, even a 1° shift in trajectory would cause a transverse deflection of over 800 AU for a 50,000 AU journey. Moreover, there could be other, unexpected sources of disturbance in the ISM, and an open-loop method could be further infeasible.

In conclusion, state-of-the-art deep space navigation technologies are inadequate for fast, interstellar spacecraft. Viable solutions to this problem are either using an autonomous navigation method that includes relativistic perturbations or designing autonomous navigation methods based on relativistic mechanics. Both approaches can solve the aforementioned issues and enable interstellar missions at relativistic speeds.

Literature review: relativistic observations

Essential work on observations on relativistic spacecraft started in 1905 with Einstein's special theory of relativity. Einstein's famous article [49] describes the relativity of lengths and times as functions of motion and derives the transformation between two distinct inertial reference frames that move with some relative velocity. A consequence of these transformations is that electromagnetic radiation emitted by an object may appear to have a different direction and wavelength/frequency/energy to a moving observer or apply a different radiation pressure on a moving reflector.

Einstein's relativistic aberration law and relativistic Doppler shift principle, in combination with the work-energy principle, describe how the approach angle of a photon and its wavelength change with relativity [49]. In 1916, Einstein generalized the special theory of relativity to include curved spacetime and gravity and named it the general theory of relativity [50]. The literature on relativistic observations focuses on different interpretations and reformulations of these two theories and describe either entirely relativistic observations or relativistic perturbations to Newtonian observations.

Entirely relativistic observations

In 1964, Oliver calculated that a set of stars uniformly distributed on a sphere appears as a prolate spheroid to a spacecraft traveling relativistically, with the spacecraft at one focus [51]. In 1991, Klioner developed a general relativistic observation model for VLBI [52]. Turyshev, in 1996, derived equations for more

general relativistic observables [53]. In 2019, Yücalan and Peck extended Einstein's special relativistic equations to describe the observed quantities in vector form, in terms of position and velocity vectors of the observer and the approach direction of the photon [54].

Relativistic perturbations to Newtonian observations

In 1992, Klioner and Kopeikin derived general relativistic corrections to time and astrometric observations [55]. In 2010, Felice et al. described the general relativistic corrections to radial velocity for measurements of the Gaia spacecraft [56]. Schuh and Behrend, in 2012, discussed special and general relativistic corrections to VLBI observations [57]. In 2014, Hees et al. discussed computation of up to second-order relativistic perturbations to time and astrometric and spectrometric observables [58]. In 2015, Titov and Girdiuk presented an alternate formula for calculating gravitational time delay in VLBI measurements [59].

Literature review: relativistic interstellar navigation

Conversely to the discussion above, astrometric, spectrometric, photometric, etc. measurements of photons by a moving observer may provide insight into the position and velocity of the observer. Accordingly, in 1975, Hoag and Wrigley suggested that an interstellar mission likely needs to measure angular directions to nearby and distant stars, Doppler shifts in the observed stellar spectra, changes in the stars' brightness and angular size, and even utilize an Earth beacon and several beacon stars, where appropriate, to be successful

[60]. Later, in 2012, Semyonov derived relativistic equations of motion and reiterated the necessity of astrometry and beacons in autonomous navigation of relativistic spacecraft [61]. The literature on relativistic interstellar navigation focuses on these observables and uses either entirely relativistic observation models or models with relativistic perturbations.

Methods based on entirely relativistic observation models

In September 2011, Calabro developed an autonomous navigation algorithm that uses astrometric measurements of quasars [62]. Bitetto, also in September 2011, described a method that uses high-frequency beacons signals to navigate [63]. In 2012, Tartaglia developed another navigation algorithm that employs both artificial and natural beacons [64]. In March 2019, Yücalan and Peck presented a relativistic autonomous navigation algorithm that calculates a spacecraft's position and velocity vectors from astrometric and spectrometric star observations, as well as the distances to observed stars [54,65]. In May 2019, Zhu et al. proposed a solution to estimate a relativistic observer's position by measuring the angular directions to three point sources [66]. In September 2019, Christian suggested methods that use Doppler effect and angular aberration measurements of three or more stars that estimate spacecraft position, velocity, and orbital elements [67]. In January 2021, Yücalan and Peck offered an optimal relativistic autonomous navigation filter that estimates spacecraft's position and velocity vectors from repeated observations [68]. Finally, in July 2021, Bailer-Jones described a method that compares onboard astrometric star measurements to a star catalog [69].

Methods based on Newtonian observation models with relativistic perturbations

In 1996, Parkinson and Spilker derived special and general relativistic corrections necessary for navigation of GPS satellites [70]. In 2001, Bahder described the general relativistic corrections to beacon signals [71]. In 2006, Sheikh et al. presented relativistic corrections for X-ray pulsar navigation [72]. Denisov, in June 2009, derived the general relativistic corrections in the laser ranging methods [73]. In July 2009, Li and Ke presented general relativistic corrections to algorithms that use pulsar ranging. Finally, in 2013, Hećimović described the effects of general relativity on time, frequency, and ranging [74].

Contributions and significance of this research

The contributions of the research presented in this dissertation to the field of aerospace engineering are four-fold.

1. This dissertation derives the relativistic autonomous observation equations, which transform the observed stars' direction vectors and characteristic wavelengths from an arbitrary inertial reference frame (e.g., that of a star catalog) to the rest frame of the spacecraft.
2. This dissertation describes a least-squares relativistic autonomous navigation algorithm based on the relativistic observation model derived in Contribution 1. This algorithm assumes that the spacecraft carries a star catalog onboard and can take astrometric and spectrometric measurements autonomously. In the end, the algorithm recursively estimates the spacecraft's position and velocity in the star catalog's reference frame, as

well as the distances to observed stars in the spacecraft's rest frame. A case study to Proxima Centauri at 20% of the speed of light assesses this algorithm's performance.

3. This dissertation describes an optimal relativistic autonomous navigation filter in the form of an extended Kalman filter based on the relativistic observation model derived in Contribution 1. This filter assumes that the spacecraft can take onboard astrometric and spectrometric measurements. The filter estimates the spacecraft's position and velocity, as well as the stars' position, velocity, and characteristic wavelength in some arbitrary inertial reference frame. The same case study described in Contribution 2 investigates this algorithm's performance.
4. This dissertation outlines a technology-push mission concept for an interstellar dark matter explorer mission that employs the two navigation algorithms outlined in Contributions 2 and 3.

Explicitly, the significance of these contributions are as follows. First, the relativistic autonomous observation equations derived in this dissertation are more general than Einstein's angle-based equations. Second, the two autonomous navigation algorithms provide a method to estimate spacecraft velocity independently from position. Third, the two autonomous navigation algorithms estimate astrometric and spectrometric quantities in addition to the spacecraft's position and velocity. Fourth, the navigation algorithms are general: they are suitable to use on any spacecraft traveling at any speed between any two points, provided the relativistic effects are detectable onboard. Fifth, the

interstellar dark matter mission suggests a near-term technology for detecting local gravitational anomalies, i.e., dark-matter anisotropy, in interstellar space using acceleration measurements.

Dissertation structure

Chapter 2 reviews relativistic concepts that inform this research. These fundamentals are a point of departure for the algorithm development in subsequent chapters.

Chapter 3 derives the relativistic autonomous observation equations, which transform astrometric and spectrometric measurables from an arbitrary inertial reference frame to the reference frame in which the spacecraft is at rest (Contribution 1).

Chapter 4 details a least-squares autonomous navigation algorithm based on the relativistic autonomous observation model, given onboard astrometric and spectrometric measurements, as well as prior knowledge of stellar kinematics. This chapter also provides a least-squares navigation algorithm based on Newtonian mechanics for comparison and simulates both algorithms under a case study (Contribution 2).

Chapter 5 describes an extended Kalman filter based on the relativistic autonomous observation model, given onboard astrometric and spectrometric measurements, as well as prior knowledge of stellar kinematics. It then assesses the algorithm's performance with a case study (Contribution 3).

Chapter 6 describes the details of a near-future interstellar mission that uses the navigation algorithms described in Chapters 4 and 5 (Contribution 4).

Chapter 7 offers a conclusion, framing the research in terms of its promise. It does so by revisiting the assumptions and limitations of the research and discusses its implications for the field of aerospace engineering.

CHAPTER 2

SUMMARY OF RELEVANT RELATIVISTIC CONCEPTS

This chapter summarizes special and general relativistic concepts that are vital for distinguishing the originality of the work presented in Chapters 3 and 6. More information about these concepts is available in relativity texts such as [18,75].

Special theory of relativity

In 1905, Albert Einstein introduced the world to the special theory of relativity and its two key postulates. First, in an inertial frame of reference, laws of physics take their simplest form. This implies that inertial frames of reference do not accelerate with respect to each other and therefore are indistinguishable from one another. Second, the speed of light in vacuum is constant and equal to c [49]. Under these postulates, the three-dimensional *space* and one-dimensional *time* combine into the four-dimensional geometry called *spacetime*. In spacetime, four numbers describe a spacetime point, or an *event*, conventionally ordered as (time, space). Moreover, a particle in spacetime travels on what is called a *worldline*.

Spacetime diagrams provide a convenient method to illustrate events and worldlines. Conventionally, in spacetime diagrams, the ordinate represents the time dimension, ct (in units of length), and the abscissa represents the space dimensions, $\boldsymbol{x} = (x, y, z)$ (in units of length). Figure 1 gives an example of such

a diagram. In the figure, particles $\mathcal{A}$ and $\mathcal{B}$ are traveling on their respective worldlines, and the point $P = (ct_P, \boldsymbol{x}_P)$ describe their rendezvous event.

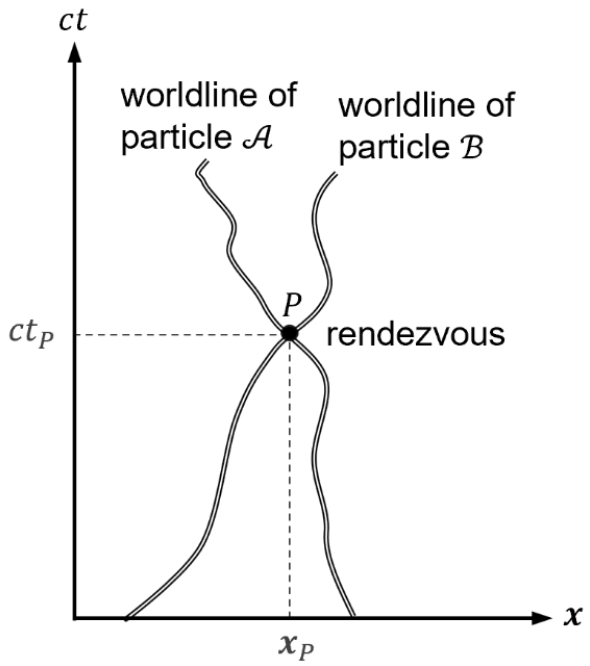

Figure 1 Spacetime diagram illustrating particles $\mathcal{A}$ and $\mathcal{B}$, their worldlines, and their rendezvous event $P = (ct_P, \boldsymbol{x}_P)$.

The special theory of relativity characterizes events by the spacetime distance, ΔS, between them. Equation (2.1) shows the calculation of the distance between two events, where Δt is the time difference between the events, Δx is the distance between the events in x coordinate, and so on.

$$\Delta S^2 = -(c\Delta t)^2 + (\Delta x)^2 + (\Delta y)^2 + (\Delta z)^2 \qquad (2.1)$$

Notice that the spacetime distance between events is a scalar quantity. Therefore, it is independent of the choice of coordinates. In other words, it is

invariant under coordinate transformations. If ΔS^2 is negative, positive, or zero, the events are called timelike-, spacelike-, and null-separated, respectively.

Connecting timelike-separated events forms a timelike worldline. All massive particles move on such worldlines. Massless particles (such as photons) travel on null worldlines. All possible null worldlines that originate from an event P form two cone-like surfaces, called *light cones*. (In four-dimensional spacetime, these surfaces are three-dimensional, hence the term cone-like.) Each event has a past light cone (pointing in the negative-time direction), and a future light cone (pointing in the positive-time direction). Figure 2 illustrates these concepts.

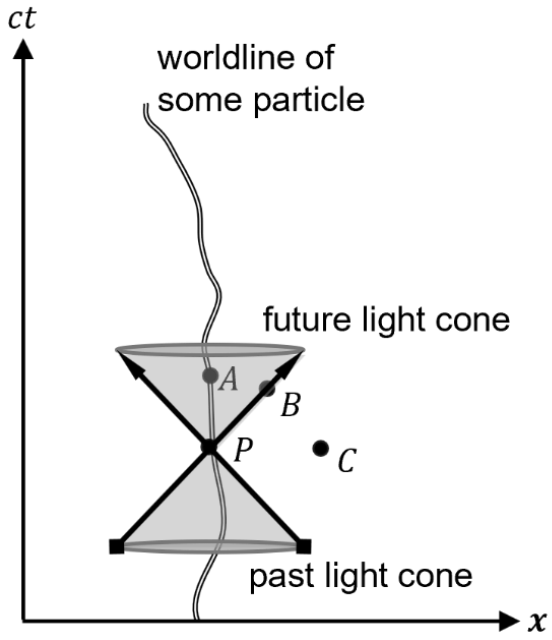

Figure 2 Spacetime diagram illustrating future and past light cones of the event P. Event P and events A, B, C are timelike-, null-, and spacelike-separated, respectively.

Light cones form the causal structure in spacetime. Thus, no information from outside a particle's past light cone can reach the particle in time, while the particle is traveling at a speed that is less than or equal to the speed of light. Then, no event outside the particle's past light cone can somehow change its behavior. Similarly, the particle cannot affect events outside its future light cone.

For example, in Figure 2, event A lies within the future light cone of the event P. This means that events P and A are timelike-separated, and that P can affect A, but not *vice versa*. In contrast, event C lies outside of both light cones, and is spacelike-separated from event P. In other words, events P and C are causally disconnected and cannot affect one another. This also implies that P and C cannot lie on the timelike or null worldlines of massless or massive particles. Finally, events P and B are null-separated, and information can travel from P to B at the speed of light, for example, via photons in vacuum.

In the four-dimensional spacetime, vectors are called four-vectors, and often denoted by Greek-letter superscript indices that run from 0 to 3. A relevant example of a four vector is the position of a particle, x^{μ}, where $\mu \in \{0, 1, 2, 3\}$. In this example, x^0 denotes the time coordinate ct, x^1 denotes the x-coordinate, x^2 denotes the y-coordinate, and so on. Another relevant example of a four-vector is the wave vector, k^{μ}, of a photon. The wave vector describes the angular frequency or wavelength of the photon in the k^0 coordinate, and the direction of motion of the photon in the k^1, k^2, and k^3 coordinates. Just like ΔS^2, norms of four-vectors are invariant under coordinate transformations.

Reference frames and their associated coordinate systems in four-dimensional spacetime are related by a series of translations, reflections, rotations, and boosts (i.e., rotation of the time dimension). The only transformations relevant to this work are boosts, and they take the general form in Equation (2.2). In this equation, d^{μ} is a four-vector in some "unprimed" reference frame, and d'^{μ} is the same four-vector, represented in the "primed" reference frame. Equation (2.2) then provides the transformation between these two reference frames. In the equation, $\boldsymbol{v} \triangleq (v_1, v_2, v_3)$ is the three-dimensional velocity of the primed reference frame relative to the unprimed reference frame, and $v = \|\boldsymbol{v}\|$, $k_{ab} = (\gamma - 1)\, v_a v_b / v^2$ for $a, b \in \{1,2,3\}$; and $\gamma = 1/\sqrt{1-\beta^2}$ for $\beta = v/c$.

$$d'^{\mu} = \begin{pmatrix} \gamma & -\gamma v_1/c & -\gamma v_2/c & -\gamma v_3/c \\ -\gamma v_1/c & k_{11}+1 & k_{12} & k_{13} \\ -\gamma v_2/c & k_{12} & k_{22}+1 & k_{23} \\ -\gamma v_3/c & k_{13} & k_{23} & k_{33}+1 \end{pmatrix} d^{\mu} \tag{2.2}$$

General theory of relativity

At its core, the general theory of relativity differs from the special theory by how it calculates the spacetime distance between two events. It does that by defining a symmetric spacetime metric tensor $g_{\mu\nu}$. This metric tensor defines a curved spacetime, in other words, $g_{\mu\nu}$ is in general a function of the two spacetime positions x^{μ} and x^{ν}. Under these definitions, Equation (2.1) turns into Equation (2.3), which now calculates the infinitesimal spacetime distance, dS, between two points separated by differential distances dx^{μ} and dx^{ν}.

$$dS^2 = \sum_{\mu,\nu=0}^{\mu,\nu=3} g_{\mu\nu} dx^\mu dx^\nu \tag{2.3}$$

Notice that if $g_{\mu\nu}$ is equal to $\eta_{\mu\nu}$ given below,

$$\eta_{\mu\nu} = \begin{pmatrix} -1 & 0 & 0 & 0 \\ 0 & 1 & 0 & 0 \\ 0 & 0 & 1 & 0 \\ 0 & 0 & 0 & 1 \end{pmatrix} \tag{2.4}$$

Then, Equation (2.3) takes the form in Equation (2.5),

$$dS^2 = -dt^2 + dx^2 + dy^2 + dz^2 \tag{2.5}$$

Which is equivalent to Equation (2.1). More simply put, the special theory of relativity is equivalent to the general theory of relativity when the spacetime metric is equal to $\eta_{\mu\nu}$. This special metric defines the flat spacetime—that in which the reference frames are inertial.

Another important concept of the general theory of relativity is Einstein's Equivalence Principle, which states that locally, a gravitational field and a corresponding acceleration of the reference system are equivalent [76]. Here, "local" describes a small enough region of the spacetime, depending on the spacetime metric. This principle implies that any curved spacetime is locally flat or inertial, in other words, all $g_{\mu\nu}$ is locally equivalent to $\eta_{\mu\nu}$.

A final important concept is gravitational time dilation, which describes the effect of approaching or receding from a massive object on time. Equation (2.6) calculates this effect, where $\Delta t'$ is the change in time in the gravitationally

influenced reference frame, Δt is the change in time in a reference frame that is infinitely distant from the massive object, G is the gravitational constant, M is the mass of the massive object, and r is the distance from the center of mass of the massive object.

$$\Delta t' = \Delta t \sqrt{1 - \frac{2GM}{rc^2}} \tag{2.6}$$

Reorganizing this equation, we see that the gravitational time dilation between two points at distances r_1 and r_2 due to a massive object is calculated by Equation (2.7).

$$\frac{\Delta t_1'}{\Delta t_2'} = \sqrt{\frac{1 - \frac{2GM}{r_1 c^2}}{1 - \frac{2GM}{r_2 c^2}}} \tag{2.7}$$

CHAPTER 3

RELATIVISTIC AUTONOMOUS OBSERVATION MODEL

This chapter derives the vector transformations of astrometric and spectrometric observables between the rest frames of a star and a spacecraft. These equations transform vectors to vectors, and reduce to Einstein's relativistic aberration law and relativistic Doppler shift principle given in Equations (3.1) and (3.2), respectively [49]. Here, v is the spacecraft's speed, c is the speed of light. ϕ is the angle between spacecraft's velocity vector and the vector connecting the star to the spacecraft in star's rest frame. ϕ' is the same angle in spacecraft's rest frame. λ, and λ' describe the wavelength of an observed photon in these two frames, respectively. Figure 3 illustrates ϕ and ϕ'.

$$\cos\phi' = \frac{\cos\phi - v/c}{1 - \cos\phi \cdot v/c} \tag{3.1}$$

$$\lambda' = \frac{\lambda}{\gamma(1 - \cos\phi \cdot v/c)} \tag{3.2}$$

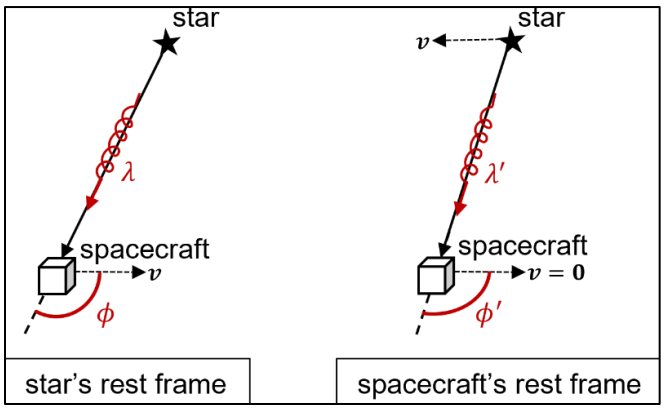

Figure 3 Einstein's definition of the variables ϕ and ϕ' in the relativistic aberration law and relativistic Doppler shift principle.

Assumptions

The most abundant objects that are observable with conventional sensors in interstellar space are stars. Onboard astrometric and spectrometric measurements can provide some information about where stars are relative to the observer and how their emission/absorption spectra appear in some range of wavelengths. Setting aside the technological specifics of cameras and spectrometers, this derivation assumes the observables available to the spacecraft are the exact directions to stars and their exact spectral signature in the rest frame of the spacecraft. This spectral signature refers to a characteristic wavelength—such as the peak wavelength—within the emission/absorption spectrum of the star that the star catalog provides. Extending this analysis to address the more general case of a full spectrum is straightforward.

Taking astrometric and spectrometric measurements in this context describes the process of receiving and inspecting photons that the stars emitted sometime in the past. In fact, exactly how long ago a star emitted a photon depends on the distance between the star (at the time of emission) and the spacecraft (at the time of observation), as well as the medium through which the photon travels. Considering how little is known about the ISM and circumstellar matter, this analysis assumes that photons do not interact with nearby matter and lose velocity [77] and considers a case where all photons travel at c. Under this condition, in this derivation, the information transfer between two events via photons happens at c.

The derivation assumes that a suitable star catalog is available onboard—one that provides the positions and characteristic wavelengths of the observed stars. Star catalogs typically use approximately inertial reference frames to establish a coordinate system in which they present their data, such as the International Celestial Reference System [78]. The analysis assumes that this reference frame is inertial. Moreover, for derivational simplicity, it assumes that the stars are at rest and perfectly known by the star catalog, and that their spectra are unchanging. In addition, it assumes that the spacecraft can recognize each star whose light it observes and match it to its entry in the star catalog.

Spacecraft traveling in the interstellar medium may experience disturbances from the environment [48]. These disturbances may cause spacecraft to accelerate in an unknown and changing direction. That said, per Einstein's equivalence principle [79], it is possible to ignore any acceleration of the spacecraft locally and approximate the spacetime as flat. As one of the goals of this work is to develop navigation algorithms for spacecraft, one can reasonably assume that the navigation algorithm can satisfy the flatness requirement by decreasing the time between estimation steps if necessary. Thus, this derivation assumes that the spacecraft is in rectilinear motion with respect to the inertial reference frame of the star catalog.

Chapters 4 and 5 discuss the effects of some of these assumptions on the navigation algorithms' performance.

Reference frames and notation

From this point forward, the *star-catalog frame* is the inertial reference frame for all the unsuperscripted quantities such as the characteristic wavelength λ_i belonging to the i[th] star, defined by the unsuperscripted coordinate system $(ct, \boldsymbol{x})$ with origin $\mathcal{C}$. In contrast, the spacecraft is at rest in its so-called *spacecraft frame*, defined by superscripted coordinates $(ct', \boldsymbol{x}')$ with origin $\mathcal{P}$, and relative to which the superscripted quantities such as the observed characteristic wavelength λ_i^o belonging to the i[th] star are defined. Note that one can choose $\mathcal{C}$ and $\mathcal{P}$ to coincide at some time t_0 without any loss of generality. Also note that all future discussions consider a single coordinate system per reference frame, both described above.

Relativistic autonomous observation equations

The system of interest under the assumptions stated earlier is equivalent to the arrangement represented in Figure 4. The figure describes the following situation. At time t, spacecraft $\mathcal{P}$ is at a position $\boldsymbol{r} = \boldsymbol{r}(t)$ in the star-catalog frame, traveling at velocity $\boldsymbol{v} = \boldsymbol{v}(t)$ from origin $\mathcal{C}$ to its destination. There exist a set of stars $\{\mathcal{S}_i \mid 1 \leq i \leq n\}$ in the sky, which are observable in both reference frames. The spacecraft $\mathcal{P}$ knows the position, $\boldsymbol{R}_i(t)$, and characteristic wavelength, $\lambda_i(t)$, of $\mathcal{S}_i$ in the star-catalog frame. $\mathcal{P}$ observes the direction to $\mathcal{S}_i$ as $\widehat{\boldsymbol{R}}_i^o(t)$ and the characteristic wavelength of $\mathcal{S}_i$ as $\lambda_i^o(t)$ in the spacecraft frame (neither visible in the figure).

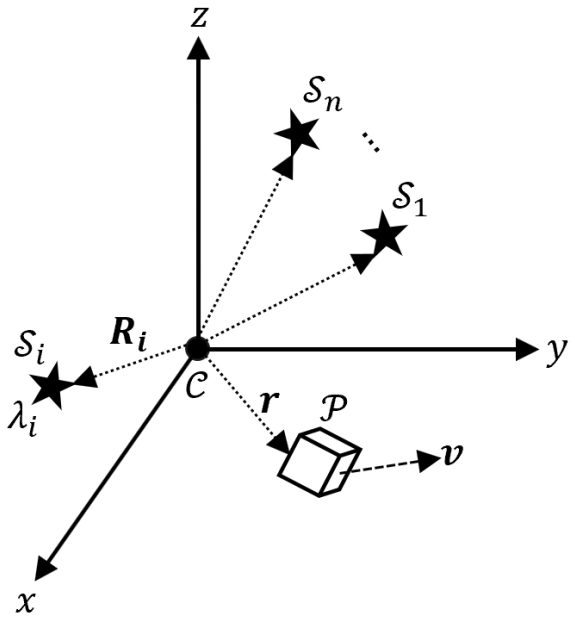

Figure 4 Relativistic autonomous observation, represented in the star-catalog frame.

Figure 5 depicts the same system in the star-catalog frame. In this reference frame, (by definition) $\mathcal{C}$ and (by assumption) $\mathcal{S}_i$ are not moving in space but are in time. As a result, their worldlines are straight lines parallel to the time axis in the figure. $\mathcal{P}$ moves (by assumption) at constant velocity $\boldsymbol{v}$, therefore its worldline is a tilted straight line: moving in space and time. Observation of a photon corresponds to the event $A = (ct, \boldsymbol{r} = \boldsymbol{v}t)$ and emission of the same photon corresponds to the event $B = (c(t - \Delta t), \boldsymbol{R}_i)$.

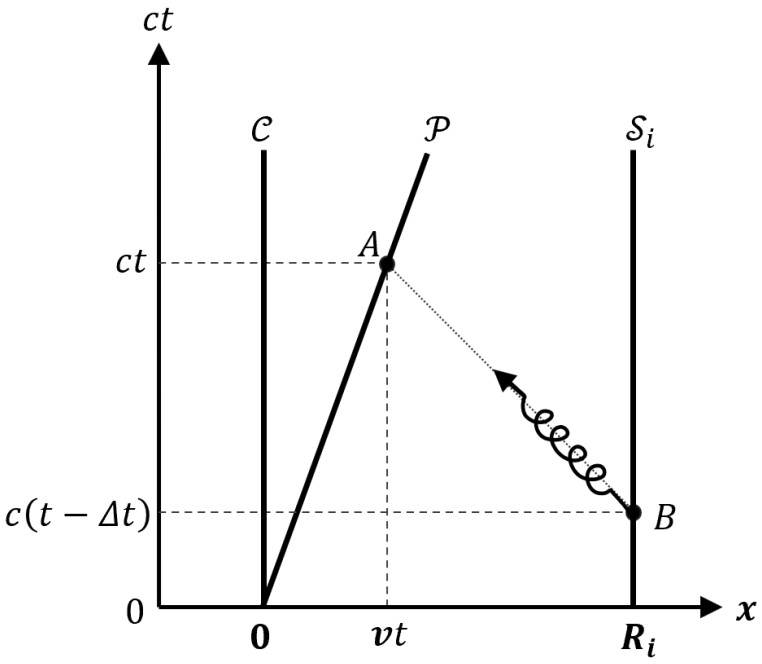

Figure 5 Relativistic autonomous observation, represented in the star-catalog frame with a spacetime diagram.

The star-catalog frame and the spacecraft frame are related by a boost, and therefore, four-vectors in those frames are related by Equation (2.2). Then, the position of some event $(t, \boldsymbol{x})$ represented in the star-catalog frame corresponds to the position $(t', \boldsymbol{x}')$ in the spacecraft frame, as described by Equations (3.3) and (3.4), for $\hat{\boldsymbol{v}} = \boldsymbol{v}/\|\boldsymbol{v}\|$.

$$t' = \gamma(t - \boldsymbol{v} \cdot \boldsymbol{x}/c^2) \tag{3.3}$$

$$\boldsymbol{x}' = \boldsymbol{x} - \gamma \boldsymbol{v} t + (\gamma - 1)(\hat{\boldsymbol{v}} \cdot \boldsymbol{x})\hat{\boldsymbol{v}} \tag{3.4}$$

Applying these transformations to spacetime coordinates of $\mathcal{C}$, $\mathcal{P}$ and $\mathcal{S}_i$, it is possible to draw worldlines of $\mathcal{C}$, $\mathcal{P}$ and $\mathcal{S}_i$ in the spacecraft frame. Figure 6

illustrates these worldlines, where $\boldsymbol{R}'_{i0} = \boldsymbol{R}_i - (1 - 1/\gamma)(\hat{\boldsymbol{v}} \cdot \boldsymbol{R}_i)\hat{\boldsymbol{v}}$, and the subscript 0—zero—represents the initial value of $\boldsymbol{R}'_i$, i.e., $\boldsymbol{R}'_i(t' = 0)$. This motion is consistent with Newtonian intuition: if $\mathcal{P}$ is moving at velocity $\boldsymbol{v}$ in the star-catalog frame, then $\mathcal{C}$ and $\mathcal{S}_i$ must be moving at velocity $-\boldsymbol{v}$ in the spacecraft frame.

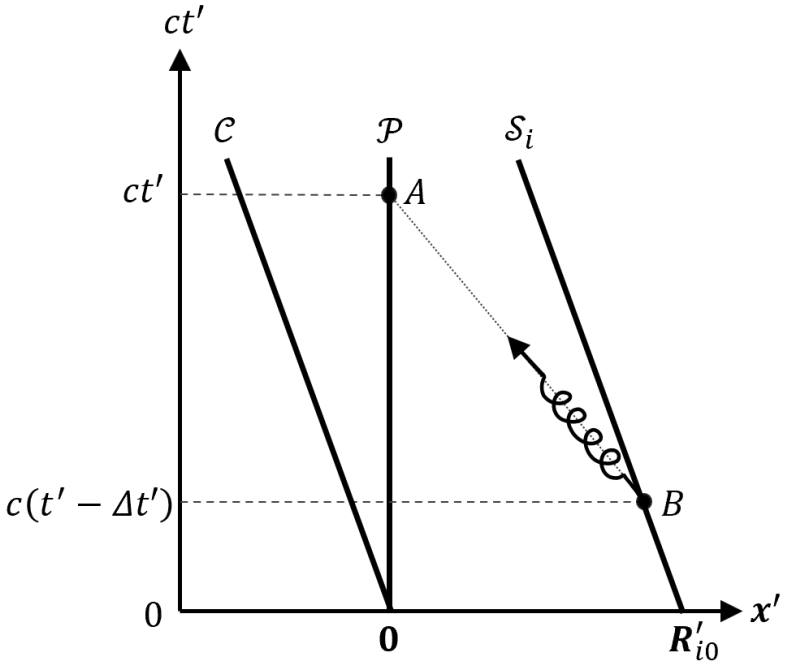

Figure 6 Relativistic autonomous observation, represented in the spacecraft frame with a spacetime diagram.

The spacetime coordinates for events A and B in the spacecraft frame are $A = (ct', \mathbf{0})$ and $B = \big(c(t' - \Delta t'), \boldsymbol{R}'_{i0} - \boldsymbol{v}(t' - \Delta t')\big)$, respectively. Since it is a photon that is traveling between A and B, these events are null-separated, and Equation (3.5) must hold.

$$0 = -(c\Delta t')^2 + \|\boldsymbol{R}'_{i0} - \boldsymbol{v}(t' - \Delta t')\|^2 \tag{3.5}$$

Solving this quadratic equation yields a single solution for $\Delta t' > 0$ (i.e., one that does not break causality), given in Equation (3.6).

$$\Delta t' = \frac{\gamma}{c}[\beta\hat{\boldsymbol{v}} \cdot (\boldsymbol{R}_i - \boldsymbol{r}) + \|\boldsymbol{R}_i - \boldsymbol{r}\|] \tag{3.6}$$

Substituting this relation to the space coordinates of B, given above as $B = \big(c(t' - \Delta t'), \boldsymbol{R}'_{i0} - \boldsymbol{v}(t' - \Delta t')\big)$, results in Equation (3.7), which gives the observed position of the star in the spacecraft frame, $\boldsymbol{R}_i^o$. The observed direction to a star in the spacecraft frame is then the unit vector $\hat{\boldsymbol{R}}_i^o$.

$$\boldsymbol{R}_i^o = \boldsymbol{R}_i - \frac{1}{\gamma}\boldsymbol{r} + (\gamma - 1)(\hat{\boldsymbol{v}} \cdot \boldsymbol{R}_i)\hat{\boldsymbol{v}} - \gamma\beta^2(\hat{\boldsymbol{v}} \cdot \boldsymbol{r})\hat{\boldsymbol{v}} + \gamma\beta\|\boldsymbol{R}_i - \boldsymbol{r}\|\hat{\boldsymbol{v}} \tag{3.7}$$

Let this observed photon have a wave four-vector $(\omega_i/c, \boldsymbol{k}_i)$ in the star-catalog frame, where ω_i is the angular frequency of the wave and $\boldsymbol{k}_i$ is the classical wave vector that points at the direction of travel. Again, this four-vector belongs to a photon and is null, and therefore, $\|\boldsymbol{k}_i\| = \omega_i/c$ must be true. Equation (2.2) again provides the transformation from the star-catalog frame to the spacecraft frame and yields the relativistic Doppler shift equation in Equation (3.8), where $\hat{\boldsymbol{k}}_i$ is the direction of travel in the star-catalog frame.

$$\omega'_i = \gamma\omega_i\big(1 - \beta\hat{\boldsymbol{v}} \cdot \hat{\boldsymbol{k}}_i\big) \tag{3.8}$$

From Figure 5, this vector corresponds to the space component of the four-vector pointing from event $B = (c(t - \Delta t), \boldsymbol{R}_i)$ to event $A = (ct, \boldsymbol{r})$, given in Equation (3.9).

$$\widehat{\boldsymbol{k}}_i = -\frac{(\boldsymbol{R}_i - \boldsymbol{r})}{\|\boldsymbol{R}_i - \boldsymbol{r}\|} \tag{3.9}$$

Substituting this relation and $\omega_i = 2\pi/\lambda_i$ into Equation (3.8) gives the observed characteristic wavelength of the star in the spacecraft frame, λ_i^o, in Equation (3.10).

$$\lambda_i^o = \lambda_i \left[\gamma\left(1 + \beta\widehat{\boldsymbol{v}} \cdot \frac{\boldsymbol{R}_i - \boldsymbol{r}}{\|\boldsymbol{R}_i - \boldsymbol{r}\|}\right)\right]^{-1} \tag{3.10}$$

Equations (3.7) and (3.10) are the relativistic autonomous observation equations.

Equivalence to Einstein's derivations

The relativistic autonomous observation equations reduce to Einstein's relativistic aberration law and relativistic Doppler shift principle, given in Equations (3.1) and (3.2). To show the equivalence, we need to write the angles ϕ and ϕ' in terms of the vector quantities defined here. In Figure 3, ϕ_i is the angle $\boldsymbol{v}$ makes with the vector pointing from $\mathcal{S}_i$ to the spacecraft in the star-catalog frame, which is equal to $-(\boldsymbol{R}_i - \boldsymbol{r})$. ϕ_i' is the same angle in the spacecraft frame. Then, Equations (3.11) and (3.12) calculate ϕ_i and ϕ_i'.

$$\cos\phi_i = \widehat{\boldsymbol{v}} \cdot \frac{-(\boldsymbol{R}_i - \boldsymbol{r})}{\|\boldsymbol{R}_i - \boldsymbol{r}\|} \tag{3.11}$$

$$\cos\phi_i' = \widehat{\boldsymbol{v}} \cdot \frac{-\boldsymbol{R}_i^o}{\|\boldsymbol{R}_i^o\|} \tag{3.12}$$

Plugging Equations (3.11) and (3.12) into Equation (3.1) and substituting β for v/c yields Equation (3.13).

$$\hat{\boldsymbol{v}} \cdot \frac{\boldsymbol{R}_i^o}{\left\|\boldsymbol{R}_i^o\right\|} = \frac{\hat{\boldsymbol{v}} \cdot \frac{(\boldsymbol{R}_i - \boldsymbol{r})}{\|\boldsymbol{R}_i - \boldsymbol{r}\|} + \beta}{1 + \beta \hat{\boldsymbol{v}} \cdot \frac{(\boldsymbol{R}_i - \boldsymbol{r})}{\|\boldsymbol{R}_i - \boldsymbol{r}\|}} \tag{3.13}$$

Taking the dot product of $\hat{\boldsymbol{v}}$ with Equation (3.7) simplifies to Equation (3.14).

$$\hat{\boldsymbol{v}} \cdot \boldsymbol{R}_i^o = \gamma \|\boldsymbol{R}_i - \boldsymbol{r}\| \left(\hat{\boldsymbol{v}} \cdot \frac{(\boldsymbol{R}_i - \boldsymbol{r})}{\|\boldsymbol{R}_i - \boldsymbol{r}\|} + \beta \right) \tag{3.14}$$

Equations (3.13) and (3.14) are equivalent if and only if Equation (3.15) is true.

$$\|\boldsymbol{R}_i^o\| = \gamma \|\boldsymbol{R}_i - \boldsymbol{r}\| + \gamma \beta \hat{\boldsymbol{v}} \cdot (\boldsymbol{R}_i - \boldsymbol{r}) \tag{3.15}$$

Taking the square of Equations (3.7) and (3.15) result identically in Equation (3.16) for $\boldsymbol{r} \parallel \boldsymbol{v}$. Therefore, Equation (3.7) is equivalent to Equation (3.1).

$$\begin{aligned} \|\boldsymbol{R}_i^o\|^2 = {} & \gamma^2 \|\boldsymbol{R}_i - \boldsymbol{r}\|^2 + \gamma^2 \beta^2 (\hat{\boldsymbol{v}} \cdot \boldsymbol{R}_i)^2 + 2\gamma^2 \beta \|\boldsymbol{R}_i - \boldsymbol{r}\| (\hat{\boldsymbol{v}} \cdot \boldsymbol{R}_i) \\ & - 2\gamma^2 \beta^2 (\hat{\boldsymbol{v}} \cdot \boldsymbol{R}_i)(\hat{\boldsymbol{v}} \cdot \boldsymbol{r}) - 2\gamma^2 \beta \|\boldsymbol{R}_i - \boldsymbol{r}\| (\hat{\boldsymbol{v}} \cdot \boldsymbol{r}) \\ & + \gamma^2 \beta^2 (\hat{\boldsymbol{v}} \cdot \boldsymbol{r})^2 \end{aligned} \tag{3.16}$$

Plugging Equation (3.11) into Equation (3.2) and substituting β for v/c yields Equation (3.17). This equation is identical to Equation (3.10). Therefore, Equation (3.10) is identical to Equation (3.2).

$$\lambda' = \frac{\lambda}{\gamma \left(1 + \beta \hat{\boldsymbol{v}} \cdot \frac{(\boldsymbol{R}_i - \boldsymbol{r})}{\|\boldsymbol{R}_i - \boldsymbol{r}\|} \right)} \tag{3.17}$$

Visualization of the equations

The relativistic autonomous observation equations in Equations (3.7) and (3.10) are different from Equation (2.2), which simply transforms spacetime positions between reference frames. The difference is easy to show in the simple example given in Figure 7. In this example, a spacecraft $\mathcal{P}$ travels at constant velocity $0.2c$ from origin $\mathcal{C}$ to Proxima Centauri, 4.24 light years from $\mathcal{C}$ in the star-catalog frame. The coordinate axes of this frame are such that the line from $\mathcal{C}$ to Proxima Centauri passes through the point $(x, y, z) = (1, 1, 1)$. At this instant, $\mathcal{P}$ is 2 light years away from $\mathcal{C}$. $\mathcal{P}$ observes two stars in addition to Proxima Centauri, both 10 light years away with static/unchanging positions in the star-catalog frame, located along the y and $-z$ axes, at distances $\mathcal{S}_y$ and $\mathcal{S}_{-z}$, respectively.

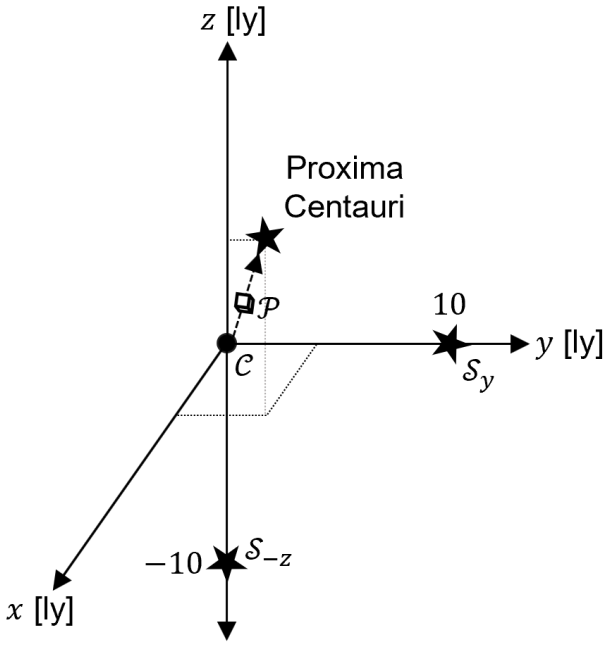

Figure 7 A simple relativistic observation example, represented in the star-catalog frame.

Traveling towards Proxima Centauri, $\mathcal{P}$ approaches $\mathcal{S}_y$ but recedes from $\mathcal{S}_{-z}$. The spacetime coordinates of all objects in the star-catalog frame are known; therefore, Equations (3.3) and (3.4) can convert these coordinates to the spacecraft frame. Table 1 gives the corresponding spacecraft-frame time coordinates (t') of the spacecraft, the two stars, and Proxima Centauri for the case where all four objects exist simultaneously in the star-catalog frame at time $t = 10$ years, at the space coordinates given above.

Table 1 Time coordinates of the spacecraft, the two stars, and Proxima Centauri in star-catalog (unprimed) and spacecraft (primed) frames for identical star-catalog frame time, t.

	t [years]	t' [years]
$\mathcal{P}$	10.0	9.80
$\mathcal{S}_{\mathrm{y}}$	10.0	9.03
$\mathcal{S}_{-\mathrm{z}}$	10.0	11.4
Proxima Centauri	10.0	9.34

The simultaneous events of $\mathcal{P}$, $\mathcal{S}_{\mathrm{y}}$, $\mathcal{S}_{-\mathrm{z}}$, and Proxima Centauri being at their positions in Figure 7 in the star-catalog frame do not represent simultaneous events in the spacecraft frame. The same is true for the reverse transformation, since that is simply Equations (3.3) and (3.4) with $v \rightarrow -v$. Table 2 gives the corresponding time coordinates of the spacecraft, the two stars, and Proxima Centauri for the case where all four exist simultaneously in the spacecraft frame at time t' = 9.80 years, which corresponds to t = 10 years for $\mathcal{P}$.

Table 2 Time coordinates of the spacecraft, the two stars, and Proxima Centauri in star-catalog (unprimed) and spacecraft (primed) frames for identical spacecraft frame time, t'.

	t [years]	t' [years]
$\mathcal{P}$	10.0	9.80
$\mathcal{S}_{\mathrm{y}}$	10.8	9.80
$\mathcal{S}_{-\mathrm{z}}$	8.38	9.80
Proxima Centauri	10.5	9.80

Table 2 implies the following: at the time of observation, objects behind the spacecraft (here, $\mathcal{S}_{-z}$) are at a past location, and objects in front of the spacecraft (here, $\mathcal{S}_{y}$ and Proxima Centauri) are at a future location. In the star-catalog frame, objects behind the spacecraft are moving away from the spacecraft. Therefore, a past location corresponds to a location nearer to the spacecraft than the nonrelativistic case where stars only shift an amount equal to spacecraft's position vector. Similarly, objects in front of the spacecraft are moving towards the spacecraft, and a future location corresponds to, again, a location nearer to the spacecraft than in the nonrelativistic case.

Figure 8 generalizes this result to many stars (at an exaggerated velocity of $0.5c$ for visualization purposes). In the figure, Newtonian frame refers to the frame of reference for which the spacecraft is at the same position, but its velocity is zero relative to the star-catalog frame. The medium-colored ellipsoid of Figure 8 shows what the spacecraft would observe if photons had infinite velocity, and the dark-colored ellipsoid shows the positions of the stars *as observed*,

calculated by Equation (3.7). Note that all observed locations correspond to past locations of the stars, and observation does not break causality. Objects behind the spacecraft "seem" nearer because the spacecraft is moving away from them, and they must send their photons earlier. Correspondingly, objects ahead "seem" farther since they continue moving after emitting the *observed* photons.

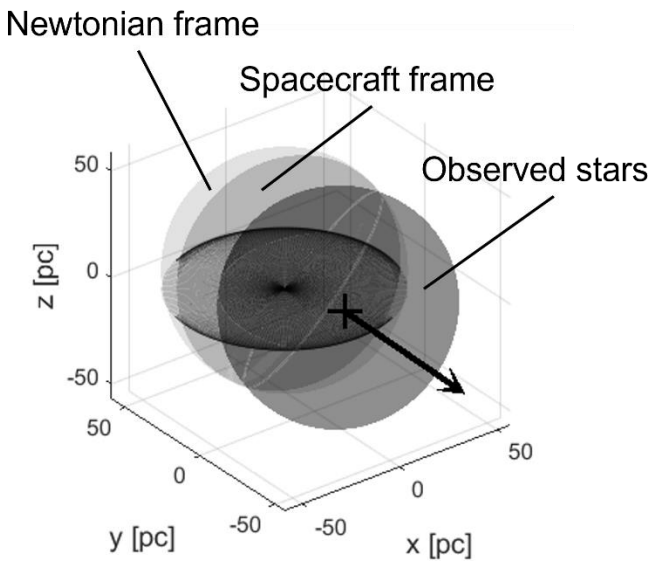

Figure 8 Stars: during observation in Newtonian frame (light-colored sphere), during observation in spacecraft frame (medium-colored ellipsoid), as observed in spacecraft frame (dark-colored ellipsoid), for $\boldsymbol{v} = 0.5c$. Plus-sign denotes the spacecraft, black arrow is parallel to spacecraft's velocity.

In addition to the position, the relativistic motion of the spacecraft also affects the observed characteristic wavelengths. Figure 9 visualizes Equation (3.10). In the figure, the ordinate represents the observed characteristic wavelengths with respect to the angle $\pi - \phi$ defined in Figure 3, for the case where the star-catalog characteristic wavelengths are all equal to 600 nm. The figure also emphasizes the visible band (380–780 nm) for visualization purposes.

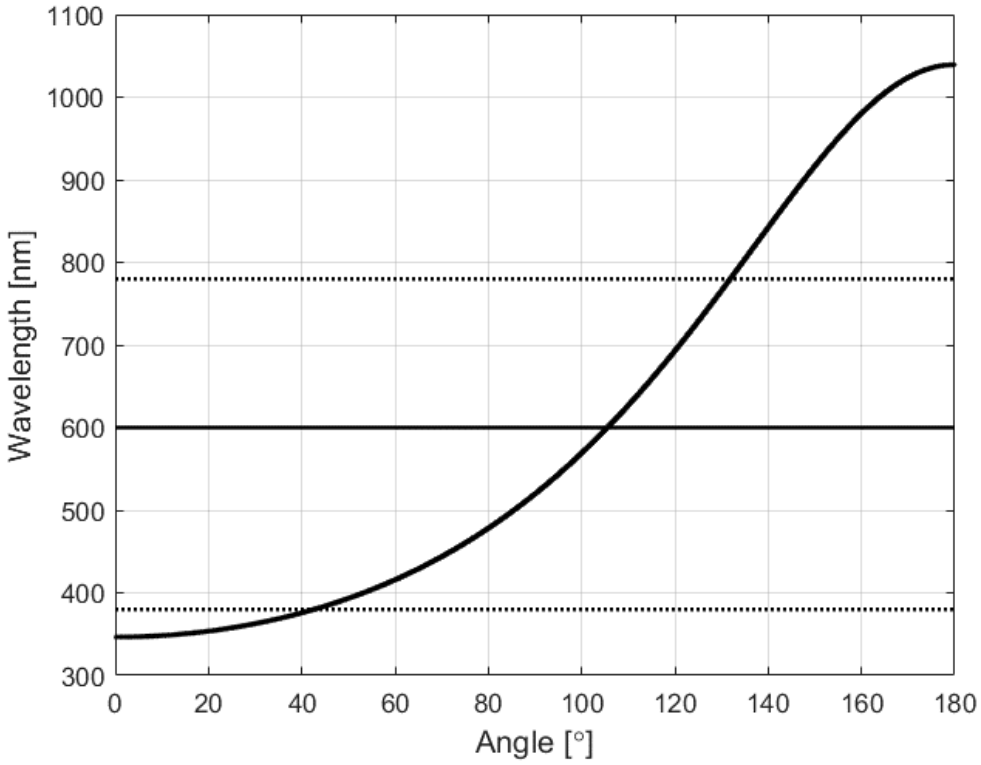

Figure 9 Observed characteristic wavelengths vs. the angle $\pi - \phi$ defined in Figure 3, for $\boldsymbol{v} = 0.5c$ and $\boldsymbol{\lambda_i} = 600$ nm (solid line). Dotted lines denote the visible band.

Conclusions

The relativistic autonomous observation equations represent a model that is traceable to modern physics. The derivations consider features of relativistic mechanics whose theory is well-understood but not directly incorporated into space technology. The existence of these equations enables novel solutions to the problem of autonomous navigation that are valid for spacecraft traveling at any speed between any two points.

CHAPTER 4

A LEAST-SQUARES APPROACH TO AUTONOMOUS NAVIGATION

This chapter describes a relativistic autonomous navigation algorithm that is based on the relativistic autonomous observation equations derived in Chapter 3. The algorithm takes advantage of the relativistic length contraction and Doppler shift of the observed star positions away from the origin to estimate the distances to the observed stars in addition to spacecraft position and velocity.

The derivations assume that the spacecraft has access to a star catalog, can take astrometric and spectrometric measurements onboard, and can recognize the stars it observes. With that, the algorithm is suitable to use for any spacecraft for which relativistic effects are detectable onboard.

A case study investigates the method in the context of technological details of a mission, including certain sources of noise and disturbance in the interstellar medium. Namely, the simulations include the measurement errors of the star catalog and the sensors, the errors in the equilibrium solution, and the random accelerations in the ISM. The chapter also derives and simulates a nonrelativistic autonomous navigation algorithm for comparison.

Assumptions

The Newtonian and relativistic autonomous navigation algorithm derivations assume that spacecraft has an onboard star catalog that provides positions and characteristic wavelengths of several stars in some inertial reference frame. They also assume that the spacecraft can take astrometric and spectrometric measurements onboard, can recognize the stars it observes, and can match the star catalog entries to the stars it observes.

Newtonian autonomous navigation algorithm

Initially, consider a nonrelativistic case. From Figure 4, we calculate the position of a star in the star-catalog frame as the sum of two vectors: the position of the spacecraft and the observed position of a star. Equation (4.1) shows this summation in terms of the variables defined in Chapter 3.

$$\boldsymbol{R}_i = \boldsymbol{r} + \boldsymbol{R}_i^o \tag{4.1}$$

Alternatively, we can derive this formula by evaluating the relativistic autonomous observation equations in the nonrelativistic limit, i.e., as $v \to 0$, and therefore $\beta \to 0$, and $\gamma \to 1$. Under these conditions, Equation (3.7) simplifies to Equation (4.1), and Equation (3.10) becomes trivial.

A linear matrix equation $Ax = b$ exists for $x \in \mathbb{R}^{(n+3)\times 1}$, given in Equation (4.2),

$$x = \begin{pmatrix} \boldsymbol{r} \\ R_1^o \\ R_2^o \\ \vdots \\ R_n^o \end{pmatrix} \tag{4.2}$$

for matrices $A \in \mathbb{R}^{(3n)\times(n+3)}$ and $b \in \mathbb{R}^{(3n)\times 1}$, given in Equations (4.3) and (4.4), where $\mathbb{I}$ denotes the identity matrix.

$$A = \begin{pmatrix} \mathbb{I} & \widehat{\boldsymbol{R}}_1^o & 0 & 0 & 0 & 0 \\ \mathbb{I} & 0 & \widehat{\boldsymbol{R}}_2^o & 0 & 0 & 0 \\ \vdots & \vdots & \ddots & \vdots & \vdots & \vdots \\ \mathbb{I} & 0 & 0 & \widehat{\boldsymbol{R}}_i^o & 0 & 0 \\ \vdots & 0 & \vdots & \vdots & \ddots & \vdots \\ \mathbb{I} & 0 & 0 & 0 & 0 & \widehat{\boldsymbol{R}}_n^o \end{pmatrix} \tag{4.3}$$

$$b = \begin{pmatrix} \boldsymbol{R}_1 \\ \boldsymbol{R}_2 \\ \vdots \\ \boldsymbol{R}_i \\ \vdots \\ \boldsymbol{R}_n \end{pmatrix} \tag{4.4}$$

The linear matrix equation can be solved $Ax = b$ with any method of linear regression [80]. This derivation considers a least-squares approach with Moore-Penrose pseudoinverse, where the solution is of the form in Equation (4.5).

$$x = (A^T A)^{-1} A^T b \tag{4.5}$$

Equations (4.2) – (4.5) represent a Newtonian autonomous navigation algorithm that estimates the position of the spacecraft and the distances to stars from the spacecraft in a common inertial frame called *the Newtonian frame* in what follows. Note that this Newtonian frame is equivalent to that in Figure 8.

Relativistic autonomous navigation algorithm

Equations (3.7) and (3.10) transform known star-catalog frame quantities ($\boldsymbol{r}$, $\boldsymbol{v}$, $\boldsymbol{R}_i$, λ_i) to the measured spacecraft frame quantities ($\widehat{\boldsymbol{R}}_i^o$, λ_i^o). However, these equations include an additional term that is neither known nor measured: R_i^o, the *distance* to the i[th] star in the spacecraft frame. As a result, it is possible (although not necessary) to estimate distances to stars in the spacecraft frame in addition to spacecraft's position and velocity.

The navigation algorithm begins with an initial guess of spacecraft's position and velocity. For example, such a guess might be based on extrapolating the trajectory via nonrelativistic orbit-mechanics. Regardless of the source of this guess, it serves as the equilibrium solution for these equations subject to small perturbations that correspond to errors in the guess. Linearizing Equations (3.7) and (3.10) around this equilibrium solution is then possible by substituting $\boldsymbol{r} = \boldsymbol{r}_e + \delta\boldsymbol{r}$, $\boldsymbol{v} = \boldsymbol{v}_e + \delta\boldsymbol{v}$, for $\|\delta\boldsymbol{r}\| \ll \|\boldsymbol{r}\|$, $\|\delta\boldsymbol{v}\| \ll \|\boldsymbol{v}\|$.

A linear matrix equation $Ax = b$ exists for $x \in \mathbb{R}^{(n+6)\times 1}$, given in Equation (4.6),

$$x = \begin{pmatrix} \delta\boldsymbol{r} \\ \delta\boldsymbol{v} \\ R_1^o \\ R_2^o \\ \vdots \\ R_n^o \end{pmatrix} \tag{4.6}$$

for matrices $A \in \mathbb{R}^{(4n)\times(n+6)}$, $b \in \mathbb{R}^{(4n)\times 1}$. Equations (4.7) – (4.14) calculate these matrices A, b by linearizing Equations (3.7) and (3.10) with $\boldsymbol{r} = \boldsymbol{r}_e + \delta\boldsymbol{r}$,

$\boldsymbol{v} = \boldsymbol{v}_e + \delta\boldsymbol{v}$, for $\|\delta\boldsymbol{r}\| \ll \|\boldsymbol{r}\|$, $\|\delta\boldsymbol{v}\| \ll \|\boldsymbol{v}\|$. The variables with subscript "e" are those evaluated at the equilibrium solution, and $\mathbb{1}$ represents the matrix of ones.

$$A = \begin{pmatrix} F_{r,1} & F_{v,1} & \widehat{\boldsymbol{R}}_1^o & \mathbf{0} & \dots & \mathbf{0} & \dots & \mathbf{0} \\ F_{r,2} & F_{v,2} & \mathbf{0} & \widehat{\boldsymbol{R}}_2^o & \dots & \mathbf{0} & \dots & \mathbf{0} \\ \vdots & \vdots & \vdots & \vdots & \dots & \vdots & \dots & \vdots \\ F_{r,i} & F_{v,i} & \mathbf{0} & \mathbf{0} & \dots & \widehat{\boldsymbol{R}}_i^o & \dots & \mathbf{0} \\ \vdots & \vdots & \vdots & \vdots & \dots & \vdots & \dots & \vdots \\ F_{r,n} & F_{v,n} & \mathbf{0} & \mathbf{0} & \dots & \mathbf{0} & \dots & \widehat{\boldsymbol{R}}_n^o \\ G_{r,1} & G_{v,1} & 0 & 0 & \dots & 0 & \dots & 0 \\ G_{r,2} & G_{v,2} & 0 & 0 & \dots & 0 & \dots & 0 \\ \vdots & \vdots & \vdots & \vdots & \dots & \vdots & \dots & \vdots \\ G_{r,i} & G_{v,i} & 0 & 0 & \dots & 0 & \dots & 0 \\ \vdots & \vdots & \vdots & \vdots & \dots & \vdots & \dots & \vdots \\ G_{r,n} & G_{v,n} & 0 & 0 & \dots & 0 & \dots & 0 \end{pmatrix} \tag{4.7}$$

$$b = \begin{pmatrix} (\boldsymbol{R}_1^o)_e \\ (\boldsymbol{R}_2^o)_e \\ \vdots \\ (\boldsymbol{R}_i^o)_e \\ \vdots \\ (\boldsymbol{R}_n^o)_e \\ \frac{\lambda_1}{\lambda_1^o} - \left(\frac{\lambda_1}{\lambda_1^o}\right)_e \\ \frac{\lambda_2}{\lambda_2^o} - \left(\frac{\lambda_2}{\lambda_2^o}\right)_e \\ \vdots \\ \frac{\lambda_i}{\lambda_i^o} - \left(\frac{\lambda_i}{\lambda_i^o}\right)_e \\ \vdots \\ \frac{\lambda_n}{\lambda_n^o} - \left(\frac{\lambda_n}{\lambda_n^o}\right)_e \end{pmatrix} \tag{4.8}$$

$$F_{r,i}\delta\boldsymbol{r} + F_{v,i}\delta\boldsymbol{v} + \widehat{\boldsymbol{R}}_i^o R_i^o \approx (\boldsymbol{R}_i^o)_e \tag{4.9}$$

$$G_{r,i}\delta\boldsymbol{r} + G_{v,i}\delta\boldsymbol{v} \approx \frac{\lambda_i}{\lambda_i^o} - \left(\frac{\lambda_i}{\lambda_i^o}\right)_e \tag{4.10}$$

$$F_{r,i} = \frac{1}{\gamma_e}\mathbb{I} + \beta_e\gamma_e\left(\beta_e\hat{\boldsymbol{v}}_e + \frac{(\boldsymbol{R}_i - \boldsymbol{r})}{\|\boldsymbol{R}_i - \boldsymbol{r}\|}\right)\hat{\boldsymbol{v}}_e^T \tag{4.11}$$

$$\begin{aligned} F_{v,i} = -\frac{1}{v_e}\Bigg\{ & \beta_e\gamma_e\|\boldsymbol{R}_i - \boldsymbol{r}_e\|(\mathbb{I} + \beta_e^2\gamma_e^2\hat{\boldsymbol{v}}_e\hat{\boldsymbol{v}}_e^T) + \frac{\beta_e^2\gamma_e^3}{c^2}\left(\hat{\boldsymbol{v}}_e^T(\boldsymbol{R}_i - \boldsymbol{r}_e)\right)\mathbb{1} \\ & - \left(\gamma_e + \frac{1}{\gamma_e} - 2\right)(\hat{\boldsymbol{v}}_e^T\boldsymbol{R}_i)\hat{\boldsymbol{v}}_e\hat{\boldsymbol{v}}_e^T + (\gamma_e - 1)(\boldsymbol{R}_i\hat{\boldsymbol{v}}_e^T + (\hat{\boldsymbol{v}}_e^T\boldsymbol{R}_i)\mathbb{I}) \\ & + \beta_e^2\gamma_e(\hat{\boldsymbol{v}}_e\boldsymbol{r}_e^T - \boldsymbol{r}_e\hat{\boldsymbol{v}}_e^T - (\hat{\boldsymbol{v}}_e^T\boldsymbol{r}_e)\mathbb{I})\Bigg\} \end{aligned} \tag{4.12}$$

$$G_{r,i} = \frac{-\beta_e\gamma_e\hat{\boldsymbol{v}}_e^T}{\|\boldsymbol{R}_i - \boldsymbol{r}_e\|}\left(\mathbb{I} - \frac{(\boldsymbol{R}_i - \boldsymbol{r}_e)(\boldsymbol{R}_i - \boldsymbol{r}_e)^T}{\|\boldsymbol{R}_i - \boldsymbol{r}_e\|^2}\right) \tag{4.13}$$

$$G_{v,i} = \frac{\gamma_e}{c}\left(\frac{(\boldsymbol{R}_i - \boldsymbol{r}_e)^T}{\|\boldsymbol{R}_i - \boldsymbol{r}_e\|} + \beta_e\gamma_e^2\left(\beta_e\frac{\hat{\boldsymbol{v}}_e^T(\boldsymbol{R}_i - \boldsymbol{r}_e)}{\|\boldsymbol{R}_i - \boldsymbol{r}_e\|} + 1\right)\hat{\boldsymbol{v}}_e^T\right) \tag{4.14}$$

Just like the nonrelativistic problem, the solution of this equation has the form in Equation (4.5). Equations (4.5) – (4.14) then represent a relativistic autonomous navigation algorithm that estimates the position and velocity of the spacecraft in the star-catalog frame and the distances to stars in the spacecraft frame.

Simulation details

The spacecraft of interest in this simulation is one that exists in the near future according to current technological trends: the Breakthrough Starshot spacecraft [28,81]. It travels in the ISM from Earth to Proxima Centauri at 20% of the speed of light, carrying onboard a star catalog, a star tracker, and a spectrometer. The star catalog provides the positions and characteristic wavelengths of some

stars, and the star tracker and spectrometer measure the directions to same stars and their characteristic wavelengths.

Though, unlike the assumptions in Chapter 3, the universe is not perfect. The star catalog and the two sensors all exhibit measurement noise. Linearizing the relativistic navigation algorithm around an equilibrium point calls for incorporating errors in the initial guesses. The interaction of the fast-moving spacecraft with the ISM disturbs the spacecraft trajectory. The following discussion summarizes how the simulations take into account these sources of error into consideration. Note that this analysis does not include technological challenges related to construction or propulsion of this spacecraft. In addition, the analysis assumes that the spacecraft carries a perfect atomic clock onboard to measure time.

Star catalog characteristics

A typical star catalog provides positions and spectral classifications of more than 100,000 stars as well as how these parameters change over time [82]. The state-of-the-art star catalog, Gaia Data Release 2, contains approximately 1.7 billion stars [83]. With this many possibilities, the number of stars used in navigation algorithms can range from 171 [84] to about 16 million [85]; the decision of the number of stars used in navigation mostly depends on the processing capabilities (note the matrix inversion in the navigation algorithms). Fortunately, demonstrating the functionality of an algorithm does not depend on the number of stars in a star catalog nor the locations of stars in the sky as those

only affect the accuracy of the results. So, for the sake of merely demonstrating functionality, these simulations consider an artificial star catalog of size 1,000.

Table 3 lists some characteristics of this set of stars. These values are comparable to the distribution of the stars in Gaia Data Release 2 with parallax 100–768.5 mas, which corresponds to stars that are within 33 light years but farther than Proxima Centauri, and with astrometric pseudo-wavelength 380–740 nm, which is an arbitrary selection. (Pseudo-wavelength is the multiplicative inverse of pseudo-color as defined by the catalog documentation, calculated using the chromatic displacements of the image centroids [85]). In the table, the starred values are slightly modified from the original to produce a more uniformly distributed catalog. All errors are assumed to be Gaussian, as established by central limit theorem. The artificial stars in this catalog are not affected by the expansion of the universe as they are within the Milky Way galaxy.

Measurement noise calculations

The right ascension error in Table 3 also represents the measurement noise for the star catalog, while the mean and standard deviation of the spectrometer's error are chosen to be 1 pm, similar to the accuracy and resolution of ESO's Very Large Telescope [86], both representing the state-of-the-art astrometric and spectrometric observation capabilities. The measurement errors are assumed to be Gaussian, as established by central limit theorem.

Table 3 Star catalog characteristics from Gaia Data Release 2.

Item	Distribution	Mean	Standard Deviation
Right ascension range [mas]	Uniform	π*	π/√3*
Right ascension error [mas]	Normal	1.1924	0.6122
Declination range [mas]	Uniform	0*	π/√12*
Declination error [mas]	Normal	1.1226	0.5856
Parallax range [mas]	Normal	236.77	50*
Parallax error [mas]	Normal	1.5757	0.8242
Proper motion in right ascension range [mas/year]	Normal	−11.517	704.04
Proper motion in right ascension error [mas/year]	Normal	2.0794	0.9800
Proper motion in declination range [mas/year]	Normal	14.302	563.07
Proper motion in declination error [mas/year]	Normal	1.8407	0.9049
Astrometric pseudo-color range [1/μm]	Normal	1.7044	0.2686
Astrometric pseudo-color error [1/μm]	Normal	0.2557	0.1288
Radial velocity error [km/s]	Normal	0.2889	0.4593

Equilibrium solution calculations

As discussed above, an equilibrium solution for spacecraft's position and velocity can come from extrapolation of the expected trajectory, since it is reasonable to expect that the spacecraft has *a priori* knowledge of its trajectory and the frequency of its observations. Equation (4.15) then provides the transformation between star-catalog time and spacecraft time which is measured perfectly onboard. This transformation is simply Equation (3.3) with

$\boldsymbol{v} \rightarrow -\boldsymbol{v}$ and $\boldsymbol{x}' = 0$ (since the spacecraft does not move in the spacecraft frame).

$$t = \gamma t' \tag{4.15}$$

Then, Equations (4.16) – (4.18) incorporate the current guess of time, velocity, and position of the spacecraft in the star-catalog frame as a function of the previous estimation, where $\Delta t'$ is the time between observations made.

$$t_e = t_{e,prev} + \gamma_e \Delta t' \tag{4.16}$$

$$v_e = v_{e,prev} \tag{4.17}$$

$$r_e = r_{e,prev} + v_{e,prev}\left(t_e - t_{e,prev}\right) \tag{4.18}$$

Star recognition problem

The simulations assume that the spacecraft recognizes each star it observed and matches these observations to the entries in the star catalog. In practice, the star-recognition–problem can be solved in any number of ways such as [87].

Interstellar medium disturbance calculations

Draine has investigated some of the environmental effects on this spacecraft in the ISM [48]. As a summary, up to ~10^{10} "standard-sized" interstellar dust particles could impact the spacecraft until it reaches its destination, Proxima Centauri, with the largest among these being ~5 μm with a mass of ~10^{-12} kg. At 20% of the speed of light, these dust particles may have momentum as high as ~10^{-2} kg m/s relative to the spacecraft, in the direction opposing the

spacecraft motion. Some of them could penetrate the spacecraft and slow it down (perfectly inelastic collision).

Table 4 gives the momentum of different-sized dust particles, the expected number of impacts during travel, and the resulting total momentum exchange for this spacecraft. The overall change in spacecraft's velocity due to these impacts ends up being ~6 km/s, which is ~0.01% of the initial velocity. It is possible to simulate this effect by inducing a uniform acceleration of magnitude approximately $10^{-10}\ \mathrm{m/s^2}$ during the mission, opposing the velocity.

Table 4 Interstellar grain impact characteristics for travel to Proxima Centauri.

Size [μm]	Mass [kg]	Momentum [kg m/s]	Expected number of impacts	Change in linear momentum of spacecraft [kg m/s]
0.1	10^{-17}	10^{-9}	10^{10}	4
1	10^{-14}	10^{-6}	10^{6}	0.7
10	10^{-11}	10^{-3}	10^{3}	0.7
100	10^{-8}	1	1	0.7

However, this effect is not the only mechanism in the ISM that would disturb the trajectory. At this velocity, the protons and electrons in the ISM have kinetic energies of magnitude ~19 MeV and ~10 keV, respectively. These energies are more than enough to eject electrons from the surface of the lightsail [88], and therefore these particles could raise the spacecraft to a positive potential. In the end, the charge accumulated on the spacecraft would be around ~1 nC.

The interstellar magnetic field strength and orientation are not well known, but its magnitude is estimated to be ~$3 \cdot 10^{-10}$ T. Lorentz force law suggests that this magnetic field would apply an acceleration with a magnitude proportional to the total spacecraft charge, spacecraft velocity, and the interstellar magnetic field strength, and inversely proportional to the spacecraft mass. This acceleration evaluates to approximately $2 \cdot 10^{-8}$ $\mathrm{m/s^2}$ during the many years of travel. Subsequently, the spacecraft's trajectory is curved with a gyroradius of ~$2 \cdot 10^{12}$ AU. This curvature would deflect the trajectory by ~0.03 AU, assuming the magnetic field direction does not change. It is then possible to simulate this effect by inducing a uniform acceleration of magnitude ~10^{-8} $\mathrm{m/s^2}$ during the trajectory, in a random direction.

General relativistic time dilation

Since this spacecraft is receding from the Sun and approaching Proxima Centauri, there will be gravitational time dilations associated with this mission. From Equation (2.7), we calculate that, if the spacecraft is leaving Earth and arriving at Proxima Centauri, the gravitational time dilation caused by the Sun is around 6.5 s over 21 years. This number is even smaller for Proxima Centauri, a star that is less massive than the Sun. This effect is significantly smaller than the effect of special relativity, which corresponds to around 5 months over 21 years. Therefore, general relativistic effects are ignored in this simulation.

With all these considerations, Figure 10 provides both the Newtonian and the relativistic algorithm simulations' flowchart for a single mission.

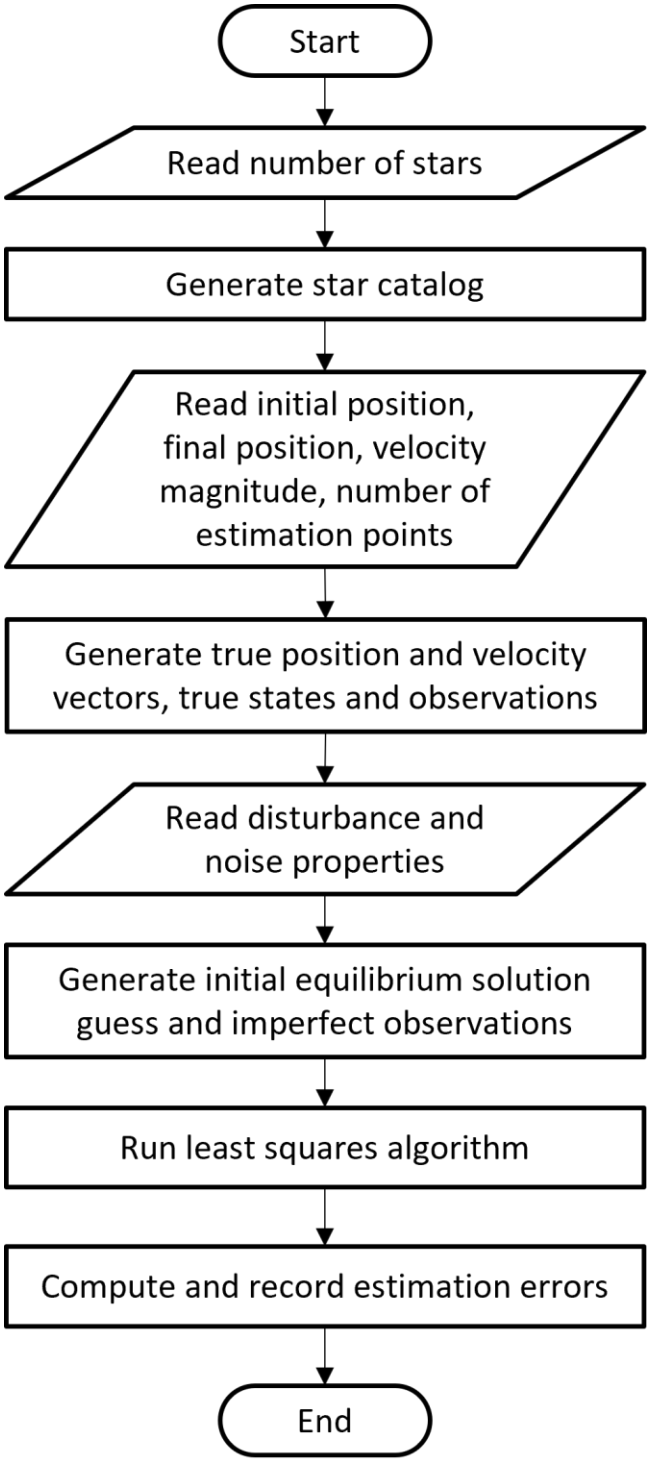

Figure 10 Flowchart of the least-squares algorithm for a single mission.

Simulation results

Both the Newtonian and relativistic autonomous navigation algorithms described in Equations (4.2) – (4.5), and Equations (4.5) – (4.14), respectively, are implemented and simulated in MATLAB version R2019b using the flowchart in Figure 10, with and without sources of error described above, at equally-separated (in time) points over the trajectory. The presented results come from Monte Carlo analyses of several runs of these algorithms with different noise values. The estimation errors discussed in the following paragraphs are averaged over estimation points and individual runs of the algorithm.

Figures 11 and 12 show results of representative run of the Newtonian navigation algorithm at 0.6 m/s and 20% of the speed of light, respectively, in an ideal universe.

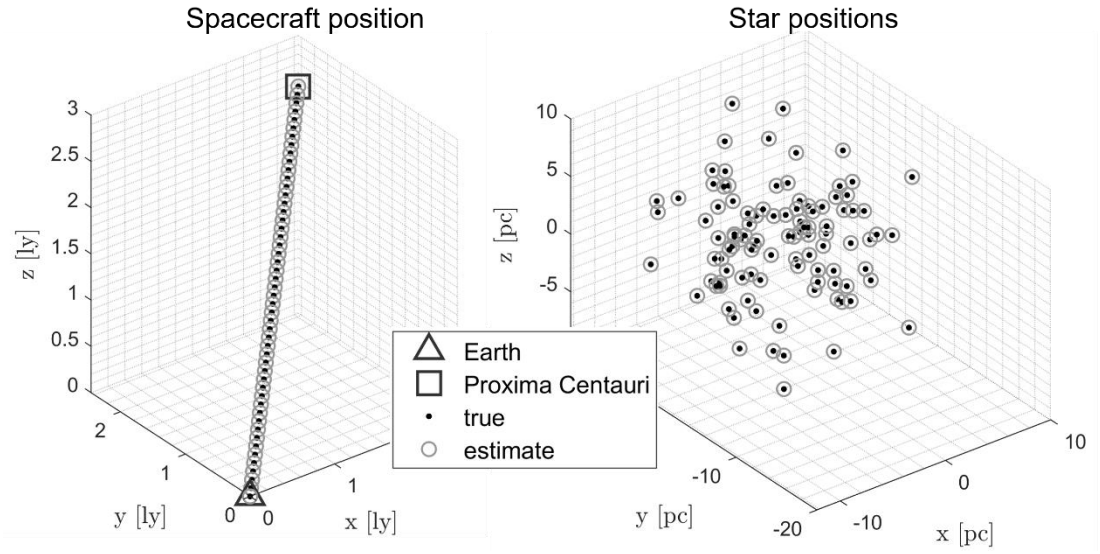

Figure 11 Representative simulation results of the Newtonian navigation algorithm for $v = 0.6\ m/s$. The visible number of stars and estimation points are reduced for visualization purposes.

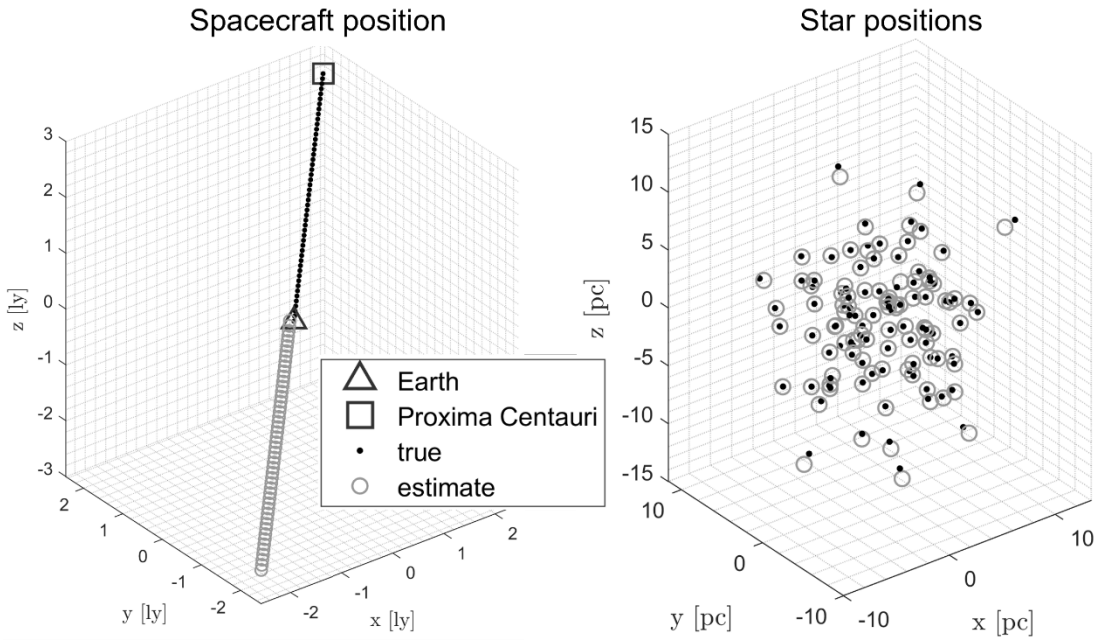

Figure 12 Representative simulation results of the Newtonian navigation algorithm for $v = 0.2c$. The visible number of stars and estimation points are reduced for visualization purposes.

Table 5 summarizes the results of the Monte Carlo simulations of the Newtonian autonomous navigation algorithm at these speeds for the ideal universe case. These results show that even at a low speed of 0.6 m/s in an ideal universe, a nonrelativistic approach to navigation exhibits an average error of approximately $3{\cdot}10^8$ m in the position of the spacecraft. Moreover, the estimation error is linear with the velocity: at 20% of the speed of light (or 10^8 times 0.6 m/s), the position error goes to around $3{\cdot}10^{16}$ m. In other words, the nonrelativistic algorithm without any perturbative corrections is unusable in the velocity regime for which interstellar travel is feasible, while the relativistic algorithm works perfectly, by definition.

Table 5 Nonrelativistic algorithm estimation errors at different spacecraft speeds (order of magnitude) for the case of zero disturbance.

	Average estimation error	
	v = 0.6 m/s	v = 0.2c
Position [m]	10^8	10^{16}
Velocity [m/s]	N/A	N/A
Distance to observed star [m]	10^7	10^{15}

Figure 13 shows results of a representative run of the relativistic autonomous navigation algorithm at 20% of the speed of light while including all the noise and disturbances mentioned earlier. Comparing Figures 12 and 13, it is clear that the relativistic algorithm performs better than the Newtonian algorithm, even after being influenced by noise and disturbance.

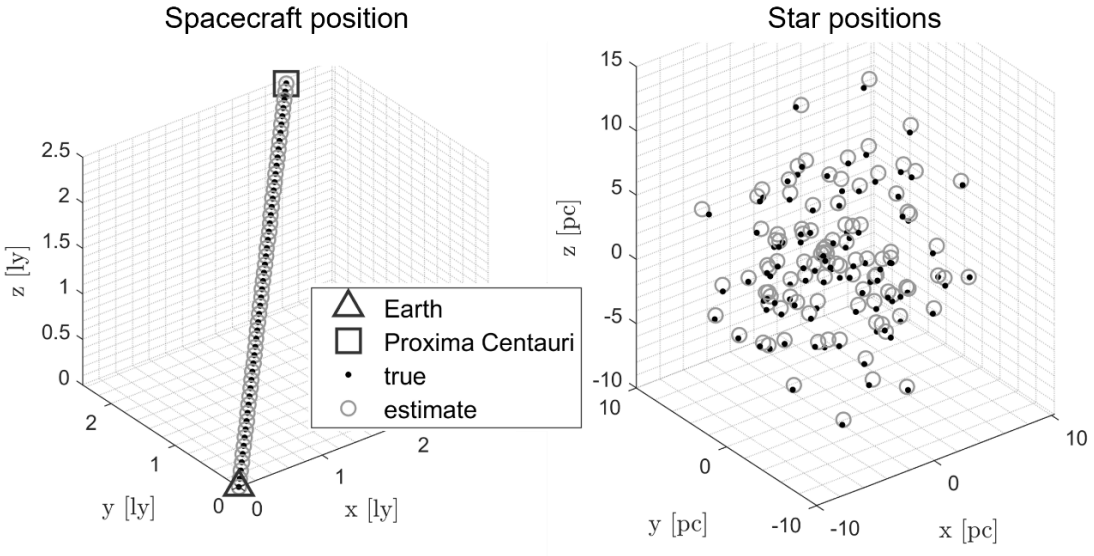

Figure 13 Representative simulation results of the relativistic navigation algorithm for $v = 0.2c$. The visible number of stars and estimation points are reduced for visualization purposes.

Table 6 then summarizes the performance of the relativistic algorithm at 20% of the speed of light while including all the noise and disturbances mentioned earlier, individually, and altogether. The relativistic autonomous observation equations are nonlinear, which explains the order-of-magnitude difference between contributions of individual and combined factors. With all these contributions, on average, the algorithm estimates the position of the spacecraft to around $4 \cdot 10^{10}$ m (%0.001 error), the velocity of the spacecraft to around 150 m/s (%0.0003 error), and the distances to stars to around $9 \cdot 10^{14}$ m (0.7% error).

Table 6 Dependence of relativistic algorithm's estimation errors on the noise and disturbance (order of magnitude).

Average estimation error	Only star motions	Only star catalog noise	Only measurement noise	Only the ISM disturbance	Only time estimation	All included
Position [m]	10^{0}	10^{-1}	10^{11}	10^{0}	10^{0}	10^{11}
Velocity [m/s]	10^{-9}	10^{-9}	10^{2}	10^{-9}	10^{-9}	10^{2}
Distance to observed star [m]	10^{-1}	10^{0}	10^{10}	10^{-1}	10^{-3}	10^{15}

As Table 6 shows, the main contributor of error in the estimation is the measurement noise of the sensors. Further simulations show that it is possible to reach a spacecraft position accuracy of around $2 \cdot 10^{9}$ m (more than an order of magnitude) with a multiplicative improvement of two in the spectrometer measurements. Similar improvements exist in estimations of spacecraft velocity and star distances. Moreover, converting the parallax range and parallax error

parameters in Table 3 to m reveals that the star catalog reports the distance to 99% of stars (3σ) with an error between $8 \cdot 10^{14}$ m and $2 \cdot 10^{16}$ m. Then, even without an improvement in the spectrometer measurements, this algorithm can enhance the accuracy of range measurements in the provided star catalog.

Figures 14 and 15 show the improvement in the algorithm performance with the addition of a simple moving average. This addition averages the error in the equilibrium solution over the previous iterations. After 1,000 iterations of the algorithm, which would correspond to a short time in a 21-year mission realistically, error between the estimated (denoted by the subscript *est*) and true position and velocity of the spacecraft reduces by more than an order of magnitude. This result implies that this algorithm shows great promise to be used as a first step in a recursive algorithm, such as a Kalman filter.

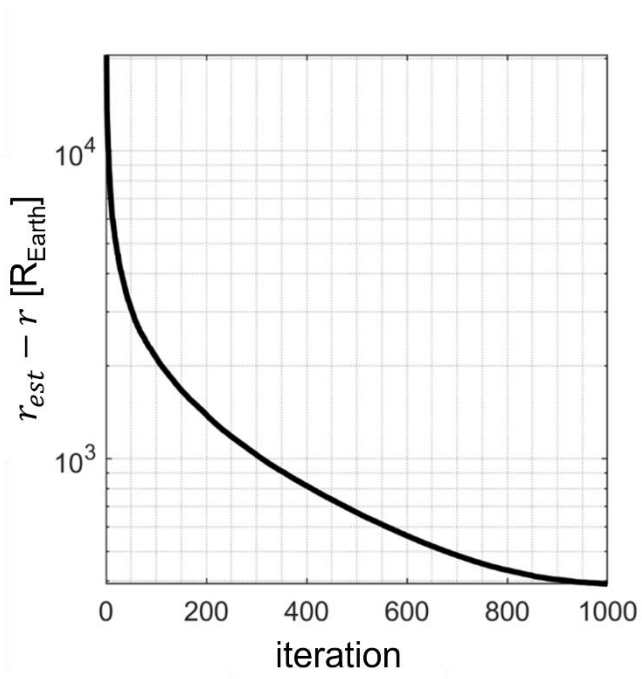

Figure 14 The change of position error with simple moving average. Each iteration represents a time step.

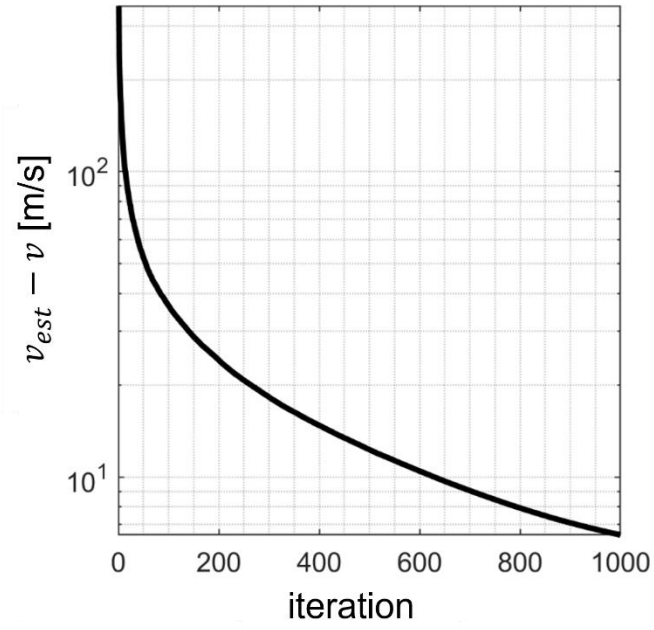

Figure 15 The change of velocity error with simple moving average. Each iteration represents a time step.

Conclusions

This study shows that not only position, but also velocity, is obtainable from star observations at relativistic speeds. The simulations of the relativistic autonomous navigation algorithm include contributions of many of the ignored factors in the derivation of the relativistic autonomous observation equations. Namely, they include the effects of the motion of stars, the imperfection of observations, the inaccurate initial guess of spacecraft's position and velocity, and interactions with the interstellar medium. Even with these sources of error involved, the navigation algorithm performs well enough to be used in any interstellar mission as a first step in a recursive algorithm, such as a Kalman filter. Moreover, the algorithm's estimating the star distances may provide means of updating the star-catalog during the mission and improve the accuracy of our current understanding of star ranges. Finally, improvements in sensor measurements betters the algorithm's accuracy significantly, which implies that future performances of this algorithm will only improve.

CHAPTER 5

AN OPTIMAL AUTONOMOUS NAVIGATION FILTER

This chapter describes an optimal relativistic autonomous navigation filter that is based on the relativistic autonomous observation equations derived in Chapter 3. The algorithm measures the relativistic length contraction and Doppler shift of the observed stars away from the origin to estimate spacecraft position and velocity, and star positions, velocities, and characteristic wavelengths.

The derivation assumes that the spacecraft has access to an inexact star catalog and imperfect sensors and can recognize the stars it observes. Moreover, it includes the acceleration of the spacecraft and motion of the stars. With these assumptions, the filter is suitable to use for any spacecraft for which relativistic effects are detectable onboard.

The same case study used in Chapter 4 investigates the method in the context of technological details of a mission, including similar sources of noise and disturbance. Specifically, the simulations include the reporting errors of the star catalog, the measurement errors of the sensors, and the random accelerations in the ISM.

Summary of an extended Kalman filter

Kalman filters use the system's dynamics and observations to calculate an optimal estimation of the states. These observations take the form of a series of sensor measurements containing noise and other inaccuracies [89]. Kalman filters, therefore, balance information obtained from dynamics and observations to estimate the state, given the uncertainty in the knowledge of the plant's dynamics and the sensors' performance.

Each Kalman filter starts by predicting the states and state covariance using dynamics. It then calculates the error in these predictions using actual observations and observation covariance. Finally, it computes a Kalman gain, a measure of trusting dynamics or observations, and uses it to update its estimate of the states and state covariance.

Extended Kalman filters specifically work with nonlinear dynamics or observations that are not linear functions of the states, as long as all nonlinear functions are smooth and differentiable. The following eight steps outline the general form of an extended Kalman filter.

1. Predict the state estimate: $x^*_{k+1,est} = f(k, x_{k,est}, \tilde{q})$
2. Predict the state covariance: $P^*_{k+1} = F_k P_k F_k^T + Q_k$, where $x^*_{k+1,est} \approx F_k x_{k,est} + \tilde{\mu}_k$ and $Q_k = E\{\tilde{\mu}_k \tilde{\mu}_k^T\}$
3. Predict the observation: $z_{k+1,est} = h(k, x^*_{k+1,est}, \tilde{r})$
4. Calculate the innovation: $y = z_{k+1} - z_{k+1,est}$

5. Calculate the innovation covariance: $S = H_k P_{k+1}^* H_k^T + R_k$, where $z_{k+1,\text{est}} \approx H_k x_{k+1,est}^* + \tilde{v}_k$ and $R_k = E\{\tilde{v}_k \tilde{v}_k{}^T\}$
6. Evaluate the Kalman gain: $K = P_{k+1}^* H_k^T S^{-1}$
7. Update the state estimate: $x_{k+1,est} = x_{k+1,est}^* + Ky$
8. Update the state covariance: $P_{k+1} = P_{k+1}^* - KH_k P_{k+1}^*$

In this formulation, the subscript "k" denotes quantities evaluated at discrete time t_k; the subscript "est" denotes estimated quantities (rather than measured); the superscript "$*$" denotes predicted quantities; "$E\{W\}$" denotes the expected value of the matrix W. With these clarifications in place, Table 7 lists the variables with the quantities they represent. The rest of this chapter focus on selecting and deriving these quantities for this filter's application.

Table 7 Extended Kalman filter variables and the quantities they represent.

Variable	Quantity
x	state vector
P	state covariance
f	state transition function
$\tilde{q}$	noise associated with unmodeled system dynamics
$\tilde{\mu}_k$	process noise
Q	process noise covariance
z	observation vector
h	observation function
$\tilde{r}$	noise associated with unmodeled observation dynamics
$\tilde{v}_k$	observation noise
R	observation noise covariance
y	innovation
K	Kalman gain

Assumptions

The optimal relativistic autonomous navigation filter derivation assumes that the spacecraft has access to onboard astrometry and spectrometry sensors can imperfectly measure directions to the same stars and their characteristic wavelengths. The star catalog is now only used to provide inexact positions, velocities, and characteristic wavelengths of several stars as initial conditions. In addition, the derivation considers a general case where the spacecraft is in uniformly accelerating motion, and the stars do not change characteristic wavelengths but move rectilinearly. Finally, the derivation ignores the star recognition problem.

Derivation of the state transition equations

Equation (5.1) provides the state vector of this filter. In summary, the states are the position, $\boldsymbol{r}_k$, and velocity, $\boldsymbol{v}_k$, of the spacecraft and the position, $\boldsymbol{R}_{i,k}$, velocity, $\boldsymbol{V}_{i,k}$, and characteristic wavelengths, $\lambda_{i,k}$ of the observed stars in the star-catalog frame at a time t_k. As a result, this vector is an element of $\mathbb{R}^{(7n+6)\times 1}$, where n is the number of observed stars.

$$x_k = \begin{pmatrix} \boldsymbol{r}_k \\ \boldsymbol{v}_k \\ \boldsymbol{R}_{1,k} \\ \vdots \\ \boldsymbol{R}_{n,k} \\ \boldsymbol{V}_{1,k} \\ \vdots \\ \boldsymbol{V}_{n,k} \\ \lambda_{1,k} \\ \vdots \\ \lambda_{n,k} \end{pmatrix} \tag{5.1}$$

Predicting the next state vector (i.e., the state vector at time t_{k+1}, or $x^*_{k+1,est}$) requires knowledge of state transition. In general, state-transition equations have the nonlinear form on the right-hand side of Step 1 of the extended Kalman filter formulation. If the spacecraft is in uniformly accelerating motion, the states $\boldsymbol{r}_k$ and $\boldsymbol{v}_k$ evolve according to Equations (5.2) and (5.3), where Δt is the time elapsed between t_k and t_{k+1}, and $\tilde{\boldsymbol{a}}$ is the random acceleration that the spacecraft experiences.

$$\boldsymbol{r}^*_{k+1,est} = \boldsymbol{r}_k + \Delta t\, \boldsymbol{v}_k + \frac{1}{2}(\Delta t)^2\, \tilde{\boldsymbol{a}} \tag{5.2}$$

$$\boldsymbol{v}^*_{k+1,est} = \boldsymbol{v}_k + \Delta t\, \tilde{\boldsymbol{a}} \tag{5.3}$$

Star catalogs have constant errors associated with their reporting of positions, velocities, and characteristic wavelengths of all n stars, denoted by variables with a tilde mark. In other words, $\boldsymbol{R}_{i,k} = \boldsymbol{R}^{true}_{i,k} + \tilde{\boldsymbol{R}}_i$, $\boldsymbol{V}_{i,k} = \boldsymbol{V}^{true}_{i,k} + \tilde{\boldsymbol{V}}_i$, and $\lambda_{i,k} = \lambda^{true}_{i,k} + \tilde{\lambda}_i$. If the stars are unchanging but moving rectilinearly, $\lambda^{true}_{i,k}$ and $\boldsymbol{V}^{true}_{i,k}$ stay constant with time, i.e., $\lambda^{true}_{i,k+1} = \lambda^{true}_{i,k}$ and $\boldsymbol{V}^{true}_{i,k+1} = \boldsymbol{V}^{true}_{i,k}$. Moreover, $\boldsymbol{R}^{true}_{i,k}$

evolves as $\boldsymbol{R}_{i,k+1}^{true} = \boldsymbol{R}_{i,k}^{true} + \Delta t\, \boldsymbol{V}_{i,k}^{true}$. From here, we can find the evolution of the rest of the states, $\boldsymbol{R}_{i,k}$, $\boldsymbol{V}_{i,k}$, and $\lambda_{i,k}$, as in Equations (5.4) – (5.6).

$$\boldsymbol{R}_{i,k+1,est}^{*} = \boldsymbol{R}_{i,k} + \Delta t\, \boldsymbol{V}_{i,k} - \Delta t\, \widetilde{\boldsymbol{V}}_{i} \tag{5.4}$$

$$\boldsymbol{V}_{i,k+1,est}^{*} = \boldsymbol{V}_{i,k} \tag{5.5}$$

$$\lambda_{i,k+1,est}^{*} = \lambda_{i,k} \tag{5.6}$$

Finding the matrices F_k and $\tilde{\mu}_k$ in Step 2 of the extended Kalman filter at this point is trivial, as Equations (5.2) – (5.6), i.e., the function f, is already linear.

Derivation of the observation equations

The observations of the spacecraft are directions and characteristic wavelengths of stars. Within the context of the relativistic autonomous observation equations in Equations (3.7) and (3.10), these quantities correspond to $\widehat{\boldsymbol{R}}_i^o$ and λ_i^o, respectively, where the "hat" operator in the former describes the unit vector parallel to the original vector. Consequently, Equation (5.7) provides the observation vector of this filter, which is an element of $\mathbb{R}^{(4n)\times 1}$.

$$z_k = \begin{pmatrix} \widehat{\boldsymbol{R}}_{1,k}^o \\ \vdots \\ \widehat{\boldsymbol{R}}_{n,k}^o \\ \lambda_{1,k}^o \\ \vdots \\ \lambda_{n,k}^o \end{pmatrix} \tag{5.7}$$

Step 3 of the extended Kalman filter predicts the observation vector from the (predicted) state estimate of Step 1. Equations (3.7) and (3.10) provide just that.

If the stars are imperfectly observed by the sensors in the spacecraft frame, Equations (5.8) – (5.10) provide the transformation from the predicted state estimate to the predicted observations (i.e., the function h), where $\widetilde{\widehat{\boldsymbol{R}}}_i^o$ and $\tilde{\lambda}_i^o$ denote the measurement errors in directions and characteristic wavelengths, respectively. Here, the quantities $\beta_{k,est}^*$, $\gamma_{k,est}^*$, and $\widehat{\boldsymbol{v}}_{k,est}^*$ denote those evaluated using $\boldsymbol{v}_{k,est}^*$. For notational simplicity, the subscripts "est" are omitted yet implied in the right-hand side quantities of Equations (5.8) – (5.10).

$$\widehat{\boldsymbol{R}}_{i,k}^o = \frac{\boldsymbol{R}_{i,k}^{o\,*}}{\left\|\boldsymbol{R}_{i,k}^{o\,*}\right\|} + \widetilde{\widehat{\boldsymbol{R}}}_i^o \tag{5.8}$$

$$\begin{aligned}\boldsymbol{R}_{i,k}^{o\,*} = \boldsymbol{R}_{i,k}^* - \frac{1}{\gamma_k^*}\boldsymbol{r}_k^* + (\gamma_k^* - 1)\left(\widehat{\boldsymbol{v}}_k^* \cdot \boldsymbol{R}_{i,k}^*\right)\widehat{\boldsymbol{v}}_k^* - \gamma_k^*(\beta_k^*)^2(\widehat{\boldsymbol{v}}_k^* \cdot \boldsymbol{r}_k^*)\widehat{\boldsymbol{v}}_k^* \\ + \gamma_k^*\beta_k^*\left\|\boldsymbol{R}_{i,k}^* - \boldsymbol{r}_k^*\right\|\widehat{\boldsymbol{v}}_k^*\end{aligned} \tag{5.9}$$

$$\lambda_{i,k}^o = \lambda_{i,k}^*\left[\gamma_k^*\left(1 + \beta_k^*\widehat{\boldsymbol{v}}_k^* \cdot \frac{\boldsymbol{R}_{i,k}^* - \boldsymbol{r}_k^*}{\left\|\boldsymbol{R}_{i,k}^* - \boldsymbol{r}_k^*\right\|}\right)\right]^{-1} + \tilde{\lambda}_{\mathrm{i}}^o \tag{5.10}$$

Finding the matrix H_k from these equations is nontrivial yet possible. Equations (5.8) – (5.10) are nonlinear, but they are smooth and differentiable for $\boldsymbol{R}_{i,k,est}^* \neq \boldsymbol{r}_{k,est}^*$, i.e., while the spacecraft is *not* traveling towards a star it observes. Then, linearize $\widehat{\boldsymbol{R}}_{i,k}^o$ and $\lambda_{i,k}^o$ about the point $t_k = 0$ (i.e., $\boldsymbol{r}_0 = \boldsymbol{0}$ and $\boldsymbol{v}_0 = \boldsymbol{0}$), and notice that $\widehat{\boldsymbol{R}}_{i,k}^o$ and $\lambda_{i,k}^o$ are equal to $\widehat{\boldsymbol{R}}_{i,k}$ and $\lambda_{i,k}$, respectively, at this point. In other words, if Equation (5.8) is equivalent to $\widehat{\boldsymbol{R}}_{i,k}^o = h_{1,i}(x_k) + \widetilde{\widehat{\boldsymbol{R}}}_i^o$, and if Equation (5.10) is equivalent to $\lambda_{i,k}^o = h_{2,i}(x_k) + \tilde{\lambda}_{\mathrm{i}}^o$, then, they are approximately equal to

Equations (5.11) and (5.12). Notice that the $\boldsymbol{V}^*_{i,k,est}$ and $\lambda^*_{i,k,est}$ terms in the linearization are trivial due to Equations (5.5) and (5.6).

$$\widehat{\boldsymbol{R}}^o_{i,k} \approx \widehat{\boldsymbol{R}}^*_{i,k,est} + \frac{\partial h_{1,i}}{\partial \boldsymbol{r}_k}\boldsymbol{r}^*_{k,est} + \frac{\partial h_{1,i}}{\partial \boldsymbol{v}_k}\boldsymbol{v}^*_{k,est} + \frac{\partial h_{1,i}}{\partial \boldsymbol{R}_k}k\Delta t\left(\boldsymbol{V}^*_{i,k,est} - \widetilde{\boldsymbol{V}}_i\right) + \widetilde{\widehat{\boldsymbol{R}}}^o_i \quad (5.11)$$

$$\lambda^o_{i,k} \approx \lambda^*_{i,k,est} + \frac{\partial h_{2,i}}{\partial \boldsymbol{r}_k}\boldsymbol{r}^*_{k,est} + \frac{\partial h_{2,i}}{\partial \boldsymbol{v}_k}\boldsymbol{v}^*_{k,est} + \frac{\partial h_{2,i}}{\partial \boldsymbol{R}_k}k\Delta t\left(\boldsymbol{V}^*_{i,k,est} - \widetilde{\boldsymbol{V}}_i\right) + \tilde{\lambda}^o_{\mathrm{i}} \quad (5.12)$$

Further notice that $\widehat{\boldsymbol{R}}^*_{i,k,est}$ is approximately equal to Equation (5.13).

$$\widehat{\boldsymbol{R}}^*_{i,k,est} \approx \left(\frac{{\boldsymbol{R}^*_{i,k,est}}^T\boldsymbol{R}^*_{i,k,est}\mathbb{I}_{3\times 3} - \boldsymbol{R}^*_{i,k,est}{\boldsymbol{R}^*_{i,k,est}}^T}{\left\|\boldsymbol{R}^*_{i,k,est}\right\|^3}\right)\Bigg|_{t_k=0}\boldsymbol{R}^*_{i,k,est} \quad (5.13)$$

Together, Equations (5.11) – (5.13) form the matrices H_k and $\tilde{v}_k$, as outlined in Equations (5.14) and (5.15), where $h_{p,i,r} \triangleq \partial h_{p,i}/\partial \boldsymbol{r}_k$, $h_{p,i,v} \triangleq \partial h_{p,i}/\partial \boldsymbol{v}_k$, $h_{p,i,R} \triangleq \partial h_{p,i}/\partial \boldsymbol{R}_k$, and Equation (5.13) is equivalent to $\widehat{\boldsymbol{R}}^*_{i,k,est} \approx M_{i,k}\boldsymbol{R}^*_{i,k,est}$.

$$H_k = \begin{pmatrix} h_{1,1,r} & h_{1,1,v} & M_{1,k} & \ddots & 0 & h_{1,1,R}k\Delta t & \ddots & 0 & 0 & \ddots \\ \vdots & \vdots & & & & & & & & \\ h_{1,n,r} & h_{1,n,v} & 0 & & M_{n,k} & 0 & & h_{1,n,R}k\Delta t & & 0 \\ h_{2,1,r} & h_{2,1,v} & 0 & & & h_{2,1,R}k\Delta t & & 0 & 1 & 0 \\ \vdots & \vdots & & \ddots & & & \ddots & & & \ddots \\ h_{2,n,r} & h_{2,n,v} & & & 0 & 0 & & h_{2,n,R}k\Delta t & 0 & 1 \end{pmatrix} \quad (5.14)$$

$$\tilde{v}_k = \begin{pmatrix} -h_{1,1,R,k}k\Delta t\widetilde{\boldsymbol{V}}_1 + \widetilde{\widehat{\boldsymbol{R}}}^o_1 \\ \vdots \\ -h_{1,n,R,k}k\Delta t\widetilde{\boldsymbol{V}}_n + \widetilde{\widehat{\boldsymbol{R}}}^o_n \\ -h_{2,1,R,k}k\Delta t\widetilde{\boldsymbol{V}}_1 + \tilde{\lambda}^o_{\mathrm{i}} \\ \vdots \\ -h_{2,n,R,k}k\Delta t\widetilde{\boldsymbol{V}}_n + \tilde{\lambda}^o_{\mathrm{i}} \end{pmatrix} \quad (5.15)$$

Simulation details

This simulation considers the same spacecraft in Chapter 4: the Breakthrough Starshot spacecraft [28,81] that travels in the ISM from Earth to Proxima Centauri at 20% of the speed of light while carrying onboard a star tracker, a spectrometer, and a perfect atomic clock. The following discussion summarizes how this simulation calculates the quantities derived earlier in the chapter, with an emphasis on the differences between Chapter 4 and this chapter.

Star catalog characteristics

The simulations in this chapter consider a catalog of 200 stars having the normally distributed characteristics listed in Table 8. The values in this table are comparable to the distribution of the 1014 stars in Gaia Early Data Release 3, which is an updated star catalog compared to that in Chapter 4 [90], with parallax 15–768.5 mas, astrometric pseudo-wavelength 380–740 nm (an arbitrary choice), and radial velocity less than or equal to 30 km/s. Different from the values in Gaia Early Data Release 3 are the distributions of right ascension and declination of the stars in the catalog. The intent here is to produce a multidirectional and uniform star catalog than what Gaia may have observed in the stellar neighborhood. Yet again, the choice to use an artificial star catalog stems from the goal of demonstrating the algorithm's functionality. All errors are assumed to be Gaussian, as established by central limit theorem.

Table 8 Star catalog characteristics, comparable to those in Gaia Data Release 2 (for radial velocity) and Gaia Early Data Release 3 (all else).

Item	Units	Variable	Distribution	Mean	Standard Deviation
Right ascension	mas	Ω	Uniform	π	π/√3
Right ascension error	mas	$\tilde{\Omega}$	Normal	0.05397	0.08863
Proper motion in right ascension	mas/year	$\dot{\Omega}$	Normal	7.7082	243.17
Proper motion in right ascension error	mas/year	$\tilde{\dot{\Omega}}$	Normal	0.07052	0.11428
Declination	mas	δ	Uniform	0	π/√12
Declination error	mas	$\tilde{\delta}$	Normal	0.05022	0.08289
Proper motion in declination	mas/year	$\dot{\delta}$	Normal	-53.493	226.99
Proper motion in declination error	mas/year	$\tilde{\dot{\delta}}$	Normal	0.06496	0.10577
Parallax	mas	p	Normal	23.985	17.387
Parallax error	mas	$\tilde{p}$	Normal	0.07104	0.11474
Radial velocity	km/s	$\dot{R}$	Normal	-7.1921	27.984
Radial velocity error	km/s	$\tilde{\dot{R}}$	Normal	0.70856	1.2873
Astrometric pseudo-color	1/μm	ν	Normal	1.47546	0.08354
Astrometric pseudo-color error	1/μm	$\tilde{\nu}$	Normal	0.01353	0.02234

The multiplicative inverse of parallax, when taken in arcseconds, provide the distance to a star (say, R_i) in parsecs. This quantity, in combination with the right ascension, declination, proper motion, and radial velocity, when taken in SI units, yield star positions and velocities, $\boldsymbol{R}_{i,0}$ and $\boldsymbol{V}_{i,0}$, respectively, in SI units, as in Equations (5.16) and (5.17). The astrometric pseudo-color yields star characteristic wavelengths, $\lambda_{i,0}$, in proper units as in Equation (5.18).

$$\boldsymbol{R}_{i,0} = R_i \begin{pmatrix} \cos\delta_i \cos\Omega_i \\ \cos\delta_i \sin\Omega_i \\ \sin\delta_i \end{pmatrix} \tag{5.16}$$

$$\boldsymbol{V}_{i,0} = \dot{R}_i \begin{pmatrix} \cos\delta_i \cos\Omega_i \\ \cos\delta_i \sin\Omega_i \\ \sin\delta_i \end{pmatrix} + R_i \begin{pmatrix} -\dot{\delta}_i \sin\delta_i \cos\Omega_i - \dot{\Omega}_i \cos\delta_i \sin\Omega_i \\ -\dot{\delta}_i \sin\delta_i \sin\Omega_i + \dot{\Omega}_i \cos\delta_i \cos\Omega_i \\ \dot{\delta}_i \cos\delta_i \end{pmatrix} \tag{5.17}$$

$$\lambda_{i,0} = \frac{1}{\nu_i} \tag{5.18}$$

The quantities tagged as “error” in Table 8 represent the measurement noise for the star catalog and contribute to the calculation of $\boldsymbol{R}_{i,0}^{true}$, $\boldsymbol{V}_{i,0}^{true}$, $\lambda_{i,0}^{true}$ as in Equations (5.19) – (5.21), where $\bar{\delta}_i = \delta_i + \tilde{\delta}_i$, $\bar{\Omega}_i = \Omega_i + \tilde{\Omega}_i$, and $\bar{R}_i = 1/(p_i + \tilde{p}_i)$ in proper units.

$$\boldsymbol{R}_{i,0}^{true} = \bar{R}_i \begin{pmatrix} \cos\bar{\delta}_i \cos\bar{\Omega}_i \\ \cos\bar{\delta}_i \sin\bar{\Omega}_i \\ \sin\bar{\delta}_i \end{pmatrix} \tag{5.19}$$

$$\boldsymbol{V}_{i,0}^{true} = \left(\dot{R}_i + \tilde{\dot{R}}_i\right)\begin{pmatrix}\cos\bar{\delta}_{i\,i}\cos\bar{\Omega}_i\\ \cos\bar{\delta}_i\sin\bar{\Omega}_i\\ \sin\bar{\delta}_i\end{pmatrix}$$

$$+\bar{R}_i\begin{pmatrix}-\left(\dot{\delta}_i+\widetilde{\dot{\delta}_\iota}\right)\sin\bar{\delta}_i\cos\bar{\Omega}_i-\left(\dot{\Omega}_i+\tilde{\dot{\Omega}}_i\right)\cos\bar{\delta}_i\sin\bar{\Omega}_i\\ -\left(\dot{\delta}_i+\widetilde{\dot{\delta}_\iota}\right)\sin\bar{\delta}_i\sin\bar{\Omega}_i+\left(\dot{\Omega}_i+\tilde{\dot{\Omega}}_i\right)\cos\bar{\delta}_i\cos\bar{\Omega}_i\\ \left(\dot{\delta}_i+\widetilde{\dot{\delta}_\iota}\right)\cos\bar{\delta}_i\end{pmatrix} \qquad (5.20)$$

$$\lambda_{i,0}^{true} = \frac{1}{\nu_i + \tilde{\nu}_i} \qquad (5.21)$$

The "error" quantities in Table 8 also inform the calculation of the star catalog error variables $\widetilde{\boldsymbol{R}}_i$, $\widetilde{\boldsymbol{V}}_i$, and $\tilde{\lambda}_i$. One can use Equations (5.16) – (5.21) to do Monte Carlo analyses that numerically yield probability distributions for these variables. Table 9 summarizes the result of these analyses done with 1,000,000 stars. The simulations assume that the star catalog errors are common for all stars and use these statistics to generate normal random numbers that represent them. These quantities are taken as Gaussian, as established by central limit theorem.

Table 9 Statistical properties of the star catalog error variables $\widetilde{\boldsymbol{R}}_i$, $\widetilde{\boldsymbol{V}}_i$, and $\tilde{\boldsymbol{\lambda}}_i$, and the measurement error variables $\widetilde{\widetilde{\boldsymbol{R}}}_i^o$ and $\tilde{\lambda}_i^o$.

Variable	Mean [m]			Standard Deviation [m]		
	x	y	z	x	y	z
$\widetilde{\boldsymbol{R}}_i$	$-1.65\cdot10^{17}$	$-1.97\cdot10^{18}$	$7.37\cdot10^{17}$	$5.64\cdot10^{20}$	$1.31\cdot10^{20}$	$5.28\cdot10^{20}$
$\widetilde{\widetilde{\boldsymbol{R}}}_i^o$	$-5.81\cdot10^{-7}$	$-1.97\cdot10^{-6}$	$6.63\cdot10^{-7}$	$7.24\cdot10^{-4}$	$1.29\cdot10^{-3}$	$5.62\cdot10^{-4}$
$\widetilde{\boldsymbol{V}}_i$	$-4.18\cdot10^{4}$	$1.46\cdot10^{4}$	$6.90\cdot10^{4}$	$3.53\cdot10^{7}$	$1.46\cdot10^{7}$	$8.82\cdot10^{7}$
$\tilde{\lambda}_i$	$-6.07\cdot10^{-9}$			$1.03\cdot10^{-8}$		
$\tilde{\lambda}_i^o$	$1\cdot10^{-12}$			$1\cdot10^{-12}$		

Measurement noise calculations

As Gaia is a state-of-the-art astrometry mission, its "error" also informs the astrometric observation noise in the simulation, $\widetilde{\widetilde{\boldsymbol{R}}}_i^o$. With a similar Monte Carlo analysis, Table 9 summarizes the characteristics of this noise. The mean and standard deviation of the spectrometric observation noise, $\tilde{\lambda}_i^o$, in the simulation are 1 pm, similar to the accuracy and resolution of the Very Large Telescope [86], a state-of-the-art spectrometer. Like the star-catalog error discussion, the simulations use the same observation error characteristics for all observations, including the assumption that these errors are Gaussian.

Star recognition problem

Same as the simulations in Chapter 4, the star recognition problem is ignored.

Interstellar medium disturbance calculations

Same as the simulations in Chapter 4, the simulation calculates the total random acceleration, $\tilde{\boldsymbol{a}}$, as the sum of these two terms: an acceleration of 10^{-10} m/s^2 that is opposing the velocity, plus an acceleration of $2{\cdot}10^{-8}$ m/s^2 in a uniform random (but constant in time) direction. This disturbance forms the process noise in the system.

General relativistic time dilation

Same as the simulations in Chapter 4, general relativistic effects are ignored.

With all these considerations, Figure 16 provides the extended Kalman filter simulations' flowchart for a single mission.

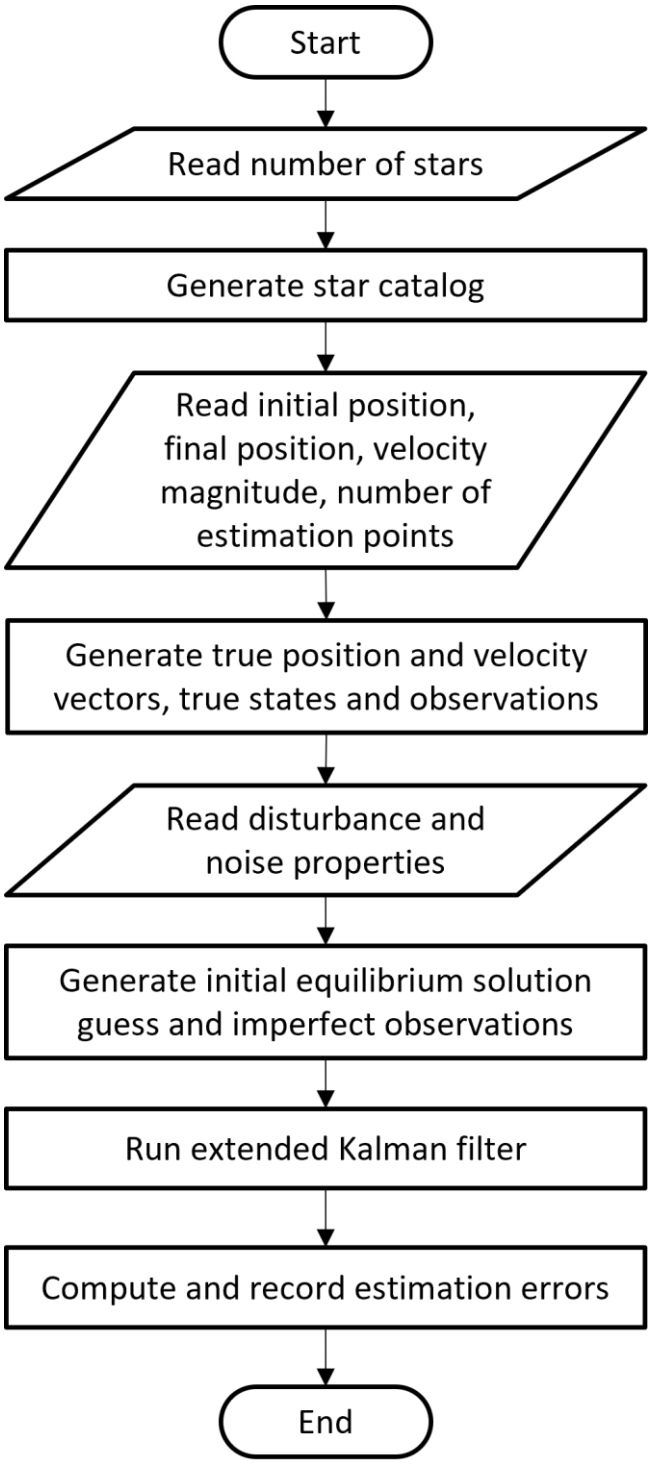

Figure 16 Flowchart of the extended Kalman filter for a single mission.

Simulation results

The rest of this chapter presents the results from Monte Carlo simulations of this optimal relativistic autonomous navigation filter. The simulation is implemented in MATLAB version R2019b using the flowchart in Figure 16, with and without process and measurement noise, at equally separated (in time) 10,000 points over the trajectory, corresponding to about one estimation/day.

Figures 17 and 18 show results of a representative run of the optimal autonomous navigation filter at 20% of the speed of light while including all the noise and disturbances mentioned earlier. Note that the time between each estimation point in these simulations is low enough that the convergence time depend only on the observability of the relativistic phenomena.

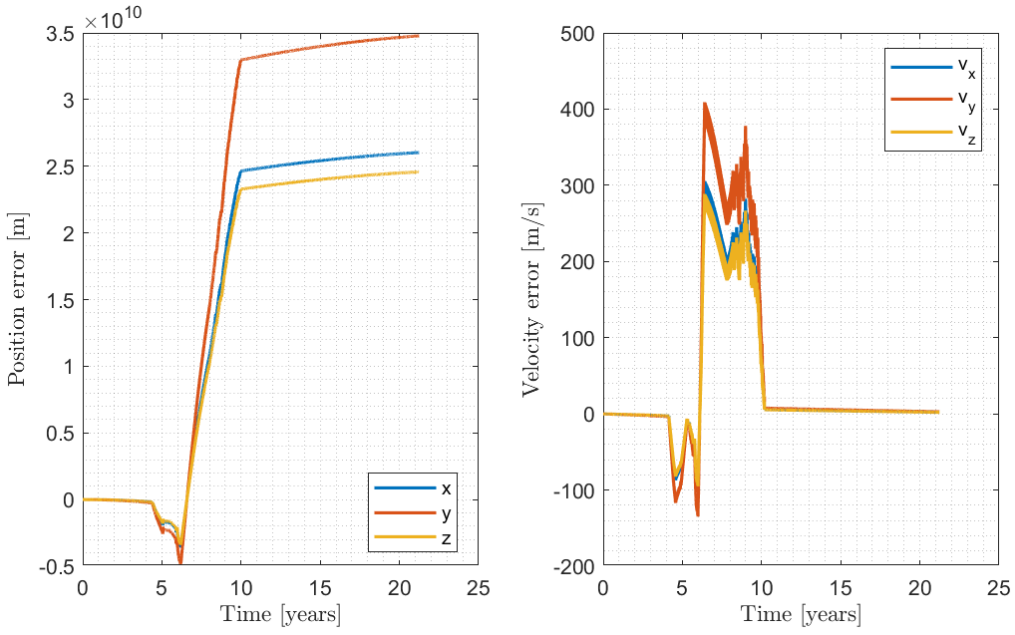

Figure 17 Estimation error convergence in position (left) and velocity (right) in a representative simulation of the optimal navigation filter for $v = 0.2c$.

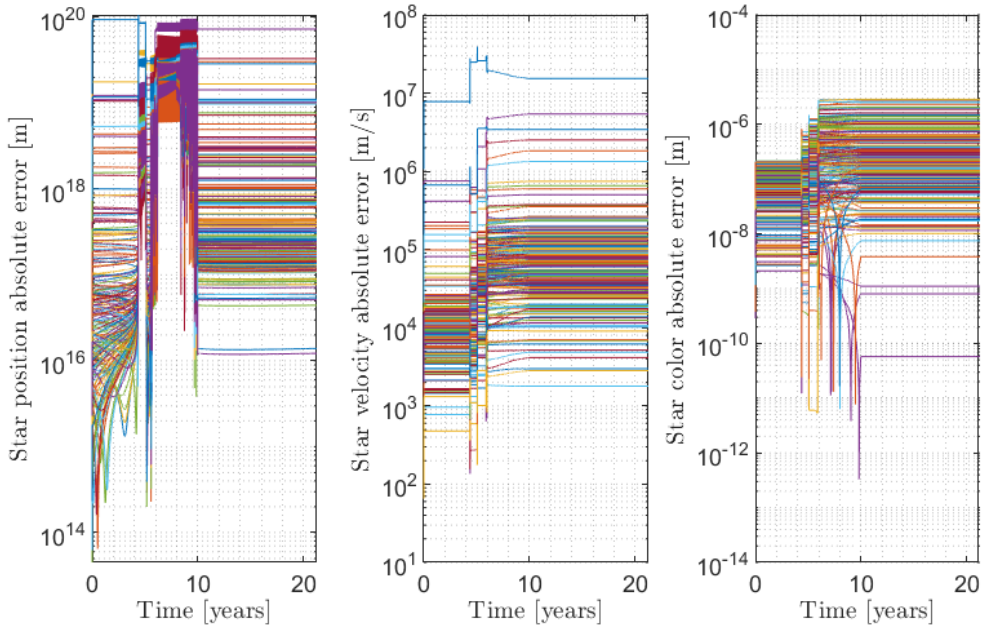

Figure 18 Estimation error convergence in star position (left), star velocity (middle), and star characteristic wavelength (right) in a representative simulation of the optimal navigation filter for $v = 0.2c$.

Table 10 summarizes the performance of the optimal algorithm at 20% of the speed of light while including all the noise and error calculated earlier, individually, and altogether. The estimation errors in this table are averaged over estimation points and individual runs of the algorithm. The relativistic autonomous observation equations are nonlinear, which explains the order-of-magnitude difference between contributions of individual and combined factors. With all these contributions, on average, the algorithm estimates the position of the spacecraft to around $4 \cdot 10^{10}$ m (%0.0002 error), the velocity of the spacecraft to around 20 m/s (%0.00003 error), star positions to around 10^{18} m, (%13 error), star velocities to around 10^{5} m/s, (%39 error), and star characteristic

wavelengths to around 10^{-7} m, (%1 error). As Table 10 shows, the main contributor of error in the spacecraft position and velocity estimation is the star catalog error, but the main contribution of error in the star positions, velocities, and characteristic wavelengths is the measurement noise.

Table 10 Dependence of optimal algorithm's estimation errors on the noise and disturbance (order of magnitude). "ϵ" denotes the numerical precision.

Average estimation error	Only process noise	Only measurement noise	Only star catalog error	All included
Position [m]	10^{4}	10^{3}	10^{9}	10^{10}
Velocity [m/s]	10^{-5}	10^{0}	10^{1}	10^{1}
Star distance [m]	10^{-10}	10^{18}	10^{13}	10^{18}
Star speed [m/s]	ϵ	10^{5}	10^{0}	10^{5}
Star characteristic wavelength [m]	ϵ	10^{-7}	10^{-12}	10^{-7}

Comparing Tables 6 and 10, we see that the optimal algorithm does at least an order of magnitude better in estimating the position and velocity of the spacecraft than the algorithm in Chapter 4, on average. However, it performs several orders of magnitude worse in estimating the distances to stars, while adding on the benefit of estimating star velocities and characteristic wavelengths. That said, converting the parameters in Table 8 to the star catalog's reporting errors, we find that the star catalog reports the distance, speed, and characteristic wavelength of 99% of stars (3σ) with errors of approximately $2{\cdot}10^{21}$ m, $7{\cdot}10^{7}$ m/s, and $2{\cdot}10^{-7}$ m, respectively. Then, even with

the state-of-the-art sensor resolutions, this algorithm can enhance the accuracy of position and velocity measurements in the provided star catalog, on average.

Conclusions

The derivation of the optimal autonomous navigation algorithm includes star motions, which were ignored in the derivation of the relativistic autonomous observation equations. Furthermore, the simulations of the filter consider other ignored effects such as star catalog errors, observation noise, and random acceleration within the interstellar medium. Even with these sources of errors involved and without the constant usage of a star catalog, the optimal filter performs better in estimating spacecraft's position and velocity than the least-squares algorithm, which is expected. What is impressive is the filter's potential in improving our current estimation accuracy of star positions and velocities. Overall, this filter shows promise as a standalone navigation filter on any interstellar mission, provided the relativistic effects are detectable onboard. Furthermore, since its estimation accuracy depends heavily on sensor measurements, future technological advances will only improve its performance, and may enable improvement in our spectrometric knowledge.

CHAPTER 6

APPLICATION: INTERSTELLAR DARK MATTER EXPLORER MISSION CONCEPT

High-level mission concept

The Interstellar Dark Matter Explorer Mission seeks to use heritage spacecraft components to detect deviations in the dark matter distribution near the heliopause within a reasonable mission duration of around 25 years. The payload utilizes ESA's GOCE spacecraft's gravity gradiometry techniques to measure local acceleration deviations with a resolution of $10^{-12}\, m/s^2$. The navigation algorithms described in Chapters 4 and 5 are used in this mission by employing ESA's Gaia spacecraft's astrometric and spectrometric techniques. NASA's Voyager spacecrafts' Communication System provide adequate downlink capabilities. SpaceX's Starship launches the spacecraft into a low Earth orbit, then the spacecraft propels itself into a hyperbolic transfer orbit to Jupiter. After performing a gravity assist maneuver around Jupiter, the spacecraft travels on another hyperbolic orbit to its destination at 125 AU from the Sun, with a total travel time of 23 years. The spacecraft operates two radioisotope thermoelectric generators, used on NASA's New Horizons spacecraft, to produce power in interstellar space. The total dry mass of the spacecraft is approximately 2.5 tons, and the Interstellar Dark Matter Explorer Mission costs less than 1.6 billion USD to develop, launch, and operate.

Science goals

Dark matter is simply matter that is non-luminous and non-absorbing. It has nonzero mass and therefore interacts with gravity. Current local and global observations suggests that the Milky Way has a dark matter halo and perhaps also a dark disk. These observations also lead one to conclude that the dark matter density near the Sun is around $6.24 \cdot 10^{-22}\ kg/m^3$, on average [91]. Recent simulations show that dark matter near the solar system could form clumps with much higher densities [19]. If so, a spacecraft that can measure gravity and that is far enough from the gravitational interactions within the solar system may be able to detect these clumps and help uncover the mystery of one of the least-understood physical phenomena. Furthermore, obtaining the dark matter distribution at a future position of the Sun may serve as a precursor for dark matter detection within the solar system in the future. The following paragraphs discuss the expected acceleration measurements for point particle and uniform sphere models of dark matter clumps.

Dark matter as point particle at a distance

The gravitational acceleration magnitude, a, applied by an infinitesimally small dark matter clump of mass M on a spacecraft that is a distance d away is calculated by Equation (6.1), where G is the gravitational constant.

$$a = \frac{GM}{d^2} \tag{6.1}$$

From Equation (6.1), we calculate the differential acceleration between two consecutive measurements at distances d_1 and $d_1 + d$ from the dark matter clump, where $d > 0$, as in Equation (6.2).

$$a_1 - a_2 = \frac{GM}{d_1^2}\left[1 - \frac{1}{(1 + d/d_1)^2}\right] \tag{6.2}$$

If $d \ll d_1$, then by using binomial approximation, we find Equation (6.2) to be approximately equal to Equation (6.3).

$$a_1 - a_2 \approx 2Gd\frac{M}{d_1^3} \tag{6.3}$$

Assuming d of the mission is known, two consecutive differential acceleration measurements yield a measure of M/d_1^3.

If the spacecraft takes n consecutive measurements, using a similar analysis, the differential acceleration between measurements i and $i + 1$ is equal to Equation (6.4).

$$a_i - a_{i+1} = \frac{GM}{d_1^2}\left[\frac{1}{[1 + (i-1)d/d_1]^2} - \frac{1}{(1 + id/d_1)^2}\right] \tag{6.4}$$

With binomial approximation, Equation (6.4) is approximately equal to Equation (6.5), which is identical to Equation (6.3). Then, all consecutive differential acceleration measurements yield a measure of M/d_1^3.

$$a_i - a_{i+1} \approx 2Gd\frac{M}{d_1^3} \tag{6.5}$$

Dark matter as uniform sphere at a distance

The discussion is similar to above, except it is now possible to express the dark matter mass as a function of density, ρ, and radius, r, of the clump sphere. In sum, all consecutive differential acceleration measurements yield a measure of $\rho(r/d_1)^3$, where d_i is the distance between the spacecraft and the clump's center of mass at measurement step i, since the differential acceleration between measurements i and $i+1$ is approximately equal to Equation (6.6).

$$a_i - a_{i+1} \approx \frac{8\pi G d}{3} \rho \left(\frac{r}{d_1}\right)^3 \tag{6.6}$$

Payload

Several missions have successfully demonstrated that sensors that measure acceleration directly or indirectly can in fact measure gravity with high precision. For example, in 2002–2017, NASA and DLR's joint mission GRACE performed gravimetry by measuring the relative distance and velocity of its twin satellites and calculating the Earth's gravitational field with a resolution of $10^{-11}\, m/s^2$ [92,93]. In 2009–2013, ESA's GOCE satellite carried three pairs of accelerometers to map Earth's gravitational anomalies using gravity gradiometry with a resolution of $10^{-12}\, m/s^2$ [94,95]. In 2012, NASA's GRAIL mission adapted GRACE's technique to the Moon [96]. In 2018, GRACE-FO replaced GRACE, and still continues to perform gravimetry around Earth [97].

Applicable to this mission concept, which requires onboard acceleration measurements, are both GRACE's gravimetry and GOCE's gravity gradiometry

techniques. Given dark matter's extremely low local-density distribution, the system that has a higher resolution should be the payload. Therefore, GOCE's Electrostatic Gravity Gradiometer (EGG) instrument, which consists of three, 50-cm apart pairs of servo-controlled, capacitive accelerometers fixed on an ultra-stable carbon-carbon structure, is proposed as the payload of this mission. This instrument will need to be calibrated in an orbit around the Earth before departing on its journey to detect dark matter, as performed originally by the GOCE spacecraft [98].

Following the dark matter models discussion, if the resolution of this instrument is $10^{-12}\ m/s^2$, then it can detect the local dark matter whenever Equation (6.7) or Equation (6.8) hold.

$$\frac{M}{d_1^3} \approx \frac{a_i - a_{i+1}}{2Gd} \geq \frac{7.5 \cdot 10^{-3}}{d} \tag{6.7}$$

$$\rho\left(\frac{r}{d_1}\right)^3 \approx \frac{a_i - a_{i+1}}{8\pi Gd/3} \geq \frac{1.8 \cdot 10^{-3}}{d} \tag{6.8}$$

Alternatively, not detecting a differential acceleration puts an upper bound on the left-hand side quantities of Equations (6.7) and (6.8).

Destination and trajectory

The requirement for this spacecraft to be located far enough from gravitational interactions within the solar system suggests that such a mission can be successful beyond the heliopause, which is around 120 AU from the Sun [99]. For example, at 125 AU, the differential gravity due to the Sun between two

accelerometers that are 50-cm apart is approximately $2.028 \cdot 10^{-20}\ m/s^2$, calculated using Equation (6.9), where $\mu_\odot = 1.327 \cdot 10^{20}\ m^3/s^2$ is the gravitational parameter of the Sun [100]. In comparison, the differential gravity at this distance due to Jupiter is approximately $1.936 \cdot 10^{-23}\ m/s^2$ for Jupiter's gravitational parameter, $\mu_J = 1.267 \cdot 10^{17}\ m^3/s^2$ [101]. These numbers are much lower than GOCE's detection accuracy. Furthermore, solar radiation pressure and related effects are virtually absent past the heliopause, by definition. Therefore, 125 AU is the operational distance from the Sun for this mission.

$$\Delta g = \mu \left(\frac{1}{r_{max}^2} - \frac{1}{r_{min}^2} \right) \tag{6.9}$$

Reaching 125 AU in less than 25 years (an arbitrary but practical goal) would require the spacecraft to travel much faster than past interstellar missions. For example, Voyager 1 reached 125 AU from the Sun in about 36 years. A common technique that increases the velocity of interstellar spacecraft to required levels is a gravity assist maneuver around Jupiter. For that, the spacecraft needs to depart Earth, travel to Jupiter on a transfer orbit, perform the gravity assist maneuver around Jupiter, and finally, depart Jupiter on an orbit that reaches 125 AU. To find the details of these orbits and the Earth departure speed relative to Earth (i.e., the launch speed), we need to work backwards and first calculate the necessary Jupiter departure velocity relative to the Sun.

Jupiter to 125 AU, hyperbolic orbit

Assume that the spacecraft travels on a hyperbolic orbit relative to the Sun after departing Jupiter to reach 125 AU as quickly as possible. Equation (6.10) calculates t, the time of flight on a hyperbolic orbit measured from the perihelion, where a denotes the semimajor axis of the orbit, r_p denotes the perihelion distance, and r denotes the position of the spacecraft from the Sun [102]. Solving this equation numerically for $t = 22\ years$, $r = 125\ AU$, and $r_p = 5.2\ AU$ results in $a = -1.295\ AU$. The perihelion choice in this calculation is arbitrary and will depend on Earth and Jupiter's relative positions during the mission.

$$t = \sqrt{\frac{(-a)^3}{\mu_\odot}}\left\{\left(1 - \frac{r_p}{a}\right)\sinh\left[\operatorname{acosh}\left(\frac{a-r}{a-r_p}\right)\right] - \operatorname{acosh}\left(\frac{a-r}{a-r_p}\right)\right\} \tag{6.10}$$

Equation (6.11), also known as the *vis-viva* equation [103], calculates the spacecraft's speed from its distance from the Sun and the semimajor axis of the orbit. From here, we find that the spacecraft's Jupiter departure speed should be 32,034 m/s relative to the Sun. Using the same equation, we find that the spacecraft's speed at 125 AU relative to the Sun is 26,443 m/s, while on this hyperbolic orbit.

$$v = \sqrt{\mu\left(\frac{2}{r} - \frac{1}{a}\right)} \tag{6.11}$$

The next unknown to solve is the spacecraft's Jupiter arrival speed before the gravity assist maneuver.

Gravity assist maneuver around Jupiter

Equation (6.12) provides the turn angle, δ, of a gravitational assist maneuver, where v_∞ is the relative velocity of the spacecraft with respect to the planet when the spacecraft is infinitely far from it, r_{fb} is the flyby radius, and μ_p is the gravitational parameter of the planet [104].

$$\sin\left(\frac{\delta}{2}\right) = \frac{1}{1 + \frac{r_{fb} v_\infty^2}{\mu_p}} \tag{6.12}$$

During a gravity assist maneuver about Jupiter, a spacecraft's departure speed relative to the Sun is maximum when its velocity vector aligns with Jupiter's orbital velocity about the Sun [104], which is equal to 13.07 km/s [101]. Then, the spacecraft's Jupiter departure (and arrival) speed relative to Jupiter should be equal to $v_\infty = 18{,}964\ m/s$. To minimize the spacecraft's arrival speed relative to the Sun given this v_∞, we need to maximize δ, or equivalently, minimize r_{fb} [104].

Take $r_{fb,min} = 75{,}600\ km$, which is the nearest approach for the Juno spacecraft's orbit' [105]. Then, from Equation (6.12), $\delta_{max} = 1.935\ rad \approx 111°$, which is also equal to the angle between Jupiter's velocity vector and the spacecraft's Jupiter entry velocity vector since the former is parallel to the spacecraft's Jupiter departure velocity. As a result, the spacecraft's Jupiter arrival speed relative to the Sun is 18,819 m/s. In other words, the net Δv relative to the Sun from this Jupiter gravity assist maneuver is 13,216 m/s. (For

comparison, Voyager 1's Δv gain around Jupiter was around 10 km/s.) The next unknown to solve is the spacecraft's Earth departure speed.

Earth to Jupiter, hyperbolic orbit

The Sun-relative speed of 18,819 m/s near Jupiter corresponds to a (barely) hyperbolic orbit about the Sun, since the escape velocity from the Sun at Jupiter's distance is 18,471 m/s, calculated from Equation (6.13).

$$v_{esc} = \sqrt{2\mu/r} \tag{6.13}$$

From Equation (6.11), this orbit corresponds to one with $a = -68.40\ AU$. From the same equation, hen this orbit crosses Earth's orbit, its orbital velocity is 42,274 m/s, which should be spacecraft's Earth departure speed relative to the Sun. The choice of other orbital parameters depends on Earth and Jupiter's positions at the time of launch and determines the time of flight from Earth to Jupiter. For instance, if this orbit's perihelion is at Earth, then, from Equation (6.10), the time of flight from Earth to Jupiter is 13.1 months, and the total time of flight from Earth to 125 AU is just over 23 years. Figure 19 illustrates the proposed spacecraft trajectory from Earth to 125 AU.

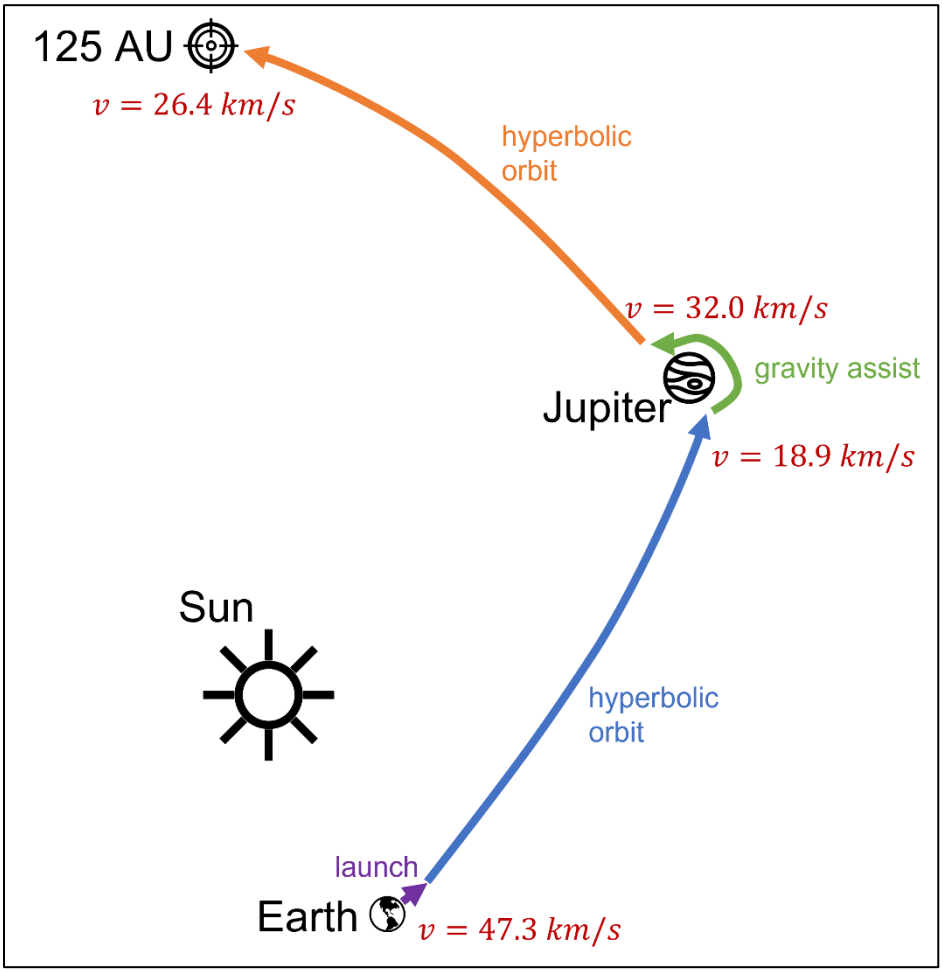

Figure 19 Illustration of the dark matter explorer spacecraft's proposed trajectory from Earth to 125 AU (not to scale). Included speeds denote spacecraft's speed relative to the Sun at points of interest.

Launch from Earth

The escape velocity from the Earth at a 500 km circular orbit (low Earth orbit, LEO) is approximately 10,771 m/s, calculated using Equation (6.13) and the gravitational parameter of Earth, $\mu_{\oplus} = 3.986 \cdot 10^{14}\ m^3/s^2$. Assuming the

spacecraft is launched from LEO in the direction of Earth's orbit around the Sun to save launch effort, given that the orbital velocity of the Earth around the Sun is 29,780 m/s on average [106], the spacecraft's launch velocity from LEO relative to the Earth is 12,494 m/s. This speed exceeds the escape velocity and corresponds to a hyperbolic orbit, which implies that the spacecraft leaves Earth's gravitational influence region (nearer than 0.01 AU [107]) relatively quickly and the calculations done without patched conic approximations [102] are acceptable for a first-order analysis. A similar discussion could be done for velocity-on-a-hyperbolic-orbit calculations near Jupiter, which has a gravitational influence region of around 0.35 AU [107].

Orbit near 125 AU

The escape velocity from the Milky Way galaxy at the Sun is estimated to be $550.9^{+32.4}_{-22.1}\ km/s$ [108]. The Sun's orbital speed about the center of the galaxy is approximately 250 km/s [100]. Then, the spacecraft's Jupiter departure orbital velocity relative to the galactic center is between 218 km/s and 282 km/s, both significantly smaller than the galactic escape velocity. This result implies that the spacecraft ultimately is in an elliptical orbit about the galactic center.

Guidance, Navigation, and Control

As mentioned earlier, the target distance for this mission is approximately 125 AU. This distance is far enough from the Earth to make the usage of DSN in navigation ineffective, as the time delay significantly affects all Earth-based ranging methods beyond heliopause. Therefore, the autonomous navigation

algorithms described in this dissertation may offer an improvement in the resolution of this dark matter exploration mission, provided that the onboard sensors can resolve the relativistic effects at this speed.

The spacecraft's speed at 125 AU relative to the Sun is 26,443 m/s. To calculate the relativistic effects this spacecraft experiences, we need to consider its motion relative to an inertial reference frame. The International Celestial Reference Frame defines itself as inertial relative to extragalactic sources [78], therefore, the extragalactic reference frame is a good inertial baseline for this purpose. We know that the Sun's orbital speed around the galactic center is approximately 250 km/s, and Milky Way's speed relative to the extragalactic reference frame is approximately 600 km/s [109]. As a result, the spacecraft's speed at 125 AU relative to an inertial reference frame is at least 823,557 m/s, which is 0.275% of the speed of light.

From Einstein's relativistic aberration law and relativistic Doppler shift principle given in Equations (3.1) and (3.2), we can calculate the change in observed angles and characteristic wavelengths at this speed. The results show that the stars may appear to move hundreds of arcseconds and may shift characteristic wavelengths in the visible region by a few nanometers. Therefore, the navigation algorithms described earlier would require onboard sensors that are able to resolve these observational changes to perform successfully throughout this mission.

ESA's Gaia spacecraft satisfy the angular and spectral resolution requirements of the navigation algorithms. Gaia's on-board star-mapper detector provides sub-arcsecond resolution for even the very faint stars [110], and its Radial Velocity Spectrometer has a resolving power of approximately 11,500 within the region 847–874 nm, which corresponds to a resolution between 73.6–76 pm. Simulating the extended Kalman filter of Chapter 5 with these observation noises and 100 stars result in an average position estimate of 70,000,000 m (0.00047 AU) and velocity estimate of 3 m/s, which is excellent performance. In sum, Gaia's Astrometric Instrument and Radial Velocity Spectrometer are the navigation sensors for this mission, providing measurements to an onboard computer that runs the optimal relativistic autonomous navigation filter, described in Chapter 5.

Detecting the acceleration due to dark matter anisotropy may require an undisturbed orbit near 125 AU. The ISM is still not well known, and the interstellar dust and gas may cause this spacecraft to accelerate significantly. In addition, the spacecraft needs a guidance system for trajectory corrections and orbital maneuvers. For these purposes, the spacecraft utilizes Gaia's Chemical Propulsion System, which uses N2O4/MMH propellant with 291 s specific impulse and 10 N nominal thrust [111].

Communications

A communication system is necessary for this spacecraft to report science data back to Earth. At a minimum, the spacecraft should send Earth its three-

dimensional position and velocity estimations from the navigation algorithm and the differential acceleration measurements from the three pairs of accelerometers.

At 130+ AU, Voyagers' antennas still successfully transfer data back to Earth, and therefore, their Communications System is a suitable option for this mission. For example, during cruise in its interstellar mission, Voyager 2 uses its High Gain Antenna in low power mode which provides downlink telemetry at 160 bps [112]—more than enough for this purpose.

Attitude Determination and Control

The spacecraft could use Gaia's telescopes as a relativistic star tracker and the acceleration readings performed by GOCE's EGG to determine its attitude [113,114]. Then, it could use Gaia's Micro Propulsion System with cold gas thrusters to control its attitude [111,115]. While many other solutions would be suitable, Gaia's offers the benefit that its size, weight, and power have already been assessed for the payload of interest, making estimates of these parameters more trustworthy.

Power and Mass

The spacecraft, at a minimum, needs to include GOCE's gravity detection and gradiometer calibration systems, Gaia's astrometry, spectrometry, orbit control, and attitude control systems, and a communication system that offers Voyager's

capability. In addition, it should include an appropriate electrical power system, onboard processing capabilities, and necessary structural elements.

Table 11 provides the power and mass budgets of the spacecraft, including roughly 25% contingency throughout per Goddard's Design Rules [116]. The total power consumption of the spacecraft, including the 25% margin in this early mission development stage [116], is estimated to be approximately 905 W. In an interstellar mission such as this, solar arrays cannot produce enough power, and nuclear power is the preferred option.

For example, the New Horizons spacecraft used a Radioisotope Thermoelectric Generator (RTG) with a mass of 56 kg, which generates 300 W at the beginning of its life, and 3.5 W less every year [117]. Then, at the end of 23 years, its power production amount becomes 219 W. Using two of these RTGs for 23 years and storing some of this power in rechargeable batteries or supercapacitors [118] for peak power consumption instances (for instance, when taking astrometric and spectrometric data) suffices for this mission.

Table 11 Power consumption and mass estimations of the included components of GOCE, Gaia, and Voyager's Communication System [24,95,119–125] and additional necessary components [24,118], including the 25% contingency margin [116].

Heritage Spacecraft Components	Function	Subsystem/Component	Power	Mass
GOCE	Gravity detection	Electrostatic Gravity Gradiometer	75 W	150 kg
	Gradiometer calibration	Gradiometer Calibration Device (cold gas thruster)	8 W	50 kg
Gaia	Astrometry and spectrometry	Astrometric Instrument and Radial Velocity Spectrometer	500 W	800 kg
	Orbit control	Chemical Propulsion System (bipropellant)	12 W	425 kg
	Attitude control	Micro Propulsion System (cold gas thruster)	12 W	60 kg
Voyager	Communication	Communication system	67 W	85 kg
Dark Matter Mission Specific Components	Data handling and processing		20 W	1 kg
	Energy storage, power management and distribution		30 W	10 kg
	Structure		-	300 kg
	Power generation (radioisotope thermoelectric generator)		-	112 kg
25% margin			181 W	499 kg
Total			**905 W**	**2492 kg**

Launch vehicle

SpaceX's Starship can deliver 150 metric tons to a 500-km orbit [126]. Including the 25% margin in this early mission development stage [116], this spacecraft has a mass of approximately 2.5 tons. Starship's capacity enables this mission to carry a high-performance chemical propulsion stage to accelerate the spacecraft to the necessary velocity for transfer orbit to Jupiter (12,494 m/s).

Specifically, the RL10B-2 engine with LOX/LH2 propellant provides an I_{sp} of 465.5 for a 5.88:1 oxidizer-to-fuel weight ratio [24]. Table 12 provides characteristic masses and densities of the RL10B-2 engine, LOX/LH2 storage tanks, and storage tank insulation.

Table 12 Characteristic masses and densities of the propulsion system [127].

RL10B-2 engine mass	663	kg
LOX density	1140	kg/m^3
LOX tank mass	12.16 × (tank volume in m^3)	kg
LOX tank insulation mass	1.123 × (tank area in m^2)	kg
LH2 density	72	kg/m^3
LH2 tank mass	9.09 × (tank volume in m^3)	kg
LH2 tank insulation mass	2.88 × (tank area in m^2)	kg

Let the LH2 mass in the LH2 tank be x kg. To minimize the mass of the tank structure and insulation, the fuel tanks are spherical. Then, from Table 12, the LH2 tank radius is $0.1491\,x^{1/3}$ m, tank mass is $0.1263\,x$ kg, and the tank

insulation mass is $0.8047\,x^{2/3}$ kg. If the engine has a 5.88:1 oxidizer-to-fuel weight ratio, the LOX mass in the LOX tank is $5.88\,x$ kg, and from Table 12, the LOX tank radius is $0.1072\,x^{1/3}$ m, tank mass is $0.0627\,x$ kg, and the tank insulation mass is $0.1621\,x^{2/3}$ kg. Then, Equations (6.14) and (6.15) provide the dry and wet masses of this spacecraft, respectively.

$$m_{dry} = 3155 + 0.1890\,x + 0.9669\,x^{2/3} \tag{6.14}$$

$$m_{wet} = 3155 + 7.0690\,x + 0.9669\,x^{2/3} \tag{6.15}$$

If the Starship can insert 150 metric tons into the desired orbit, then the maximum value of x is 20,670 kg, which means the total dry mass is 7,790 kg, and the total propellant mass is 142,210 kg. Equation (6.16), the Tsiolkovsky rocket equation, calculates the Δv this spacecraft can achieve with this amount of LOX/LH2, as 13,502 m/s, which is 1008 m/s higher than the required speed, 12,494 m/s. This extra Δv represents propellant mass margin.

$$\Delta v = I_{sp} g_0 \ln \frac{m_{wet}}{m_{dry}} \tag{6.16}$$

GOCE's and Gaia's dimensions are 5.3 m × 2.3 m and 4.6 m × 2.3 m, respectively. The propulsion engine RL10B-2's dimensions are 4.15 m × 2.15 m. From Table 12, the LOX and LH2 tanks' diameters are 5.88 m and 8.18 m, respectively. Starship's payload volume dimensions has a diameter of 8 m, and a height of up to 22 m [126], and can comfortably accommodate all components of the spacecraft.

Cost

Table 13 provides the individual costs of the heritage elements of this mission and estimates the total cost of this mission to be less than 1.6 billion USD. This cost is about half the expected development cost of NASA's Nancy Grace Roman Space Telescope, to be launched in 2027 [128]. The real cost is expected to be lower than 1.6 billion USD, as this solution excludes the development of individual instruments.

Table 13 Top-level individual costs of the heritage elements included in this spacecraft [117,129–135].

Item	**Cost**
GOCE spacecraft (including operations)	$325,560,000
Gaia spacecraft (including operations)	$698,258,000
Voyager spacecraft (including operations)	$360,000,000
2 x New Horizons RTG	$260,000,000
Starship launch	$10,000,000
Total	**$1,653,818,000**

Conclusions

This technology-push dark matter explorer mission concept employs well-understood and space-demonstrated technology of several heritage spacecraft. It proposes a new idea to detect deviations in the dark matter distribution within the solar system. Utilizing the relativistic autonomous navigation algorithms presented in the earlier chapters and GOCE's excellent performance, this mission looks promising even in this early development stage. Advancing the analyses presented in this chapter may help the physics community understand a fundamental unknown of our universe.

CHAPTER 7

CONCLUSION

This dissertation focuses on spacecraft traveling relativistically in interstellar space, particularly the problem of its navigation. The problem arises because the state-of-the-art Earth-based navigation, as well as the autonomous navigation methods developed around Newtonian mechanics are insufficient for relativistic interstellar missions. This dissertation seeks to solve this problem by developing autonomous navigation algorithms framed around relativistic mechanics. It does so by first modeling the observations of this spacecraft, then developing autonomous navigation algorithms around this observation model, and finally, presenting a mission concept that uses the relativistic autonomous navigation methods and investigating the methods' performance.

The relativistic autonomous observation model derived in Chapter 3 has many simplifying assumptions. It assumes that the spacecraft is in uniform rectilinear motion, the stars it observes are static, the star catalog reports observed stars' positions and characteristic wavelengths exactly, and its onboard sensors take perfect measurements. With these assumptions, Chapter 3 derives an observation model that is more general than Einstein's angle-based equations—used commonly by other researchers for developing relativistic methods.

The relativistic autonomous navigation methods described in Chapters 4 and 5 establish around the relativistic observation model in Chapter 3. In derivations

and simulations, these methods relax many of Chapter 3's assumptions, and successfully estimate the spacecraft's position and velocity to a reasonable degree. In addition, these methods provide a novel way of improving our current astrometric and spectrometric capabilities. Furthermore, both methods are generally suitable for any spacecraft at any speed between any two points, provided it is equipped by adequate sensors.

Chapter 6 describes a technology-push mission concept for an interstellar dark matter explorer mission that employs well-understood and space-demonstrated technology of heritage spacecraft and the relativistic navigation algorithms of Chapters 4 and 5. This mission concept suggests a technology for detecting dark-matter anisotropy in interstellar space using acceleration measurements, which has never been done before.

In sum, this dissertation provides a more general observation model than what is currently used in the field of aerospace engineering, which can enhance the development of relativistic navigation algorithms and other relativistic calculations. Additionally, this dissertation describes two general autonomous navigation algorithms which show that not only position, but also velocity, is obtainable from star observations at relativistic speeds. Both algorithms are suitable for all spacecraft traveling at any speed and on any trajectory and can improve our astrometric and spectrometric knowledge base. Finally, dark matter is a highly sought-after topic of interest in the physics and space communities, and this dissertation offers a near-term technology for answering some of their

questions. For these reasons, this dissertation represents broad impact to the field of aerospace engineering.

REFERENCES

[1] Gurnett, D. A., Kurth, W. S., et al. “In Situ Observations of Interstellar Plasma with Voyager 1.” *Science*, Vol. 341, No. 6153, 2013, pp. 1489–1492. https://doi.org/10.1126/science.1241681.

[2] Jet Propulsion Laboratory. Voyager. *Voyager*. https://voyager.jpl.nasa.gov/. Accessed Sep. 8, 2019.

[3] Jet Propulsion Laboratory. Voyager - The Interstellar Mission. *Voyager*. https://voyager.jpl.nasa.gov/mission/interstellar-mission/. Accessed May 11, 2022.

[4] Jet Propulsion Laboratory. Voyager - Interstellar Science. *Voyager*. https://voyager.jpl.nasa.gov/mission/science/. Accessed May 11, 2022.

[5] European Space Agency Gaia Collaboration. “The Gaia Mission.” *Astronomy & Astrophysics*, Vol. 595, 2016, p. A1. https://doi.org/10.1051/0004-6361/201629272.

[6] Cordiner, M. A., Linnartz, H., et al. “Confirming Interstellar C 60 + Using the Hubble Space Telescope.” *The Astrophysical Journal*, Vol. 875, No. 2, 2019, p. L28. https://doi.org/10.3847/2041-8213/ab14e5.

[7] Anglada-Escudé et al., G., Butler, R. P., et al. “A Terrestrial Planet Candidate in a Temperate Orbit around Proxima Centauri.” *Nature*, Vol. 536, No. 7617, 2016, pp. 437–440. https://doi.org/10.1038/nature19106.

[8] AMS Collaboration, Aguilar, M., et al. “First Result from the Alpha Magnetic Spectrometer on the International Space Station: Precision Measurement of the Positron Fraction in Primary Cosmic Rays of 0.5--350 GeV.” *Physical Review Letters*, Vol. 110, No. 14, 2013, p. 141102. https://doi.org/10.1103/PhysRevLett.110.141102.

[9] Trimble, V. “Existence and Nature of Dark Matter in the Universe.” *Annual Reviews of Astronomy and Astrophysics*, Vol. 25, 1987, pp. 425–472. https://doi.org/10.1146/annurev.aa.25.090187.002233.

[10] de Swart, J. G., Bertone, G., et al. “How Dark Matter Came to Matter.” *Nature Astronomy*, Vol. 1, No. 3, 2017, p. 0059. https://doi.org/10.1038/s41550-017-0059.

[11] Hu, W., and White, M. “The Cosmic Symphony.” *Scientific American*, 2004. https://doi.org/10.1038/scientificamerican0204-44.

[12] Hubble Detects Smallest Known Dark Matter Clumps. *HubbleSite.org*. http://hubblesite.org/contents/news-releases/2020/news-2020-05. Accessed Jun. 20, 2022.

[13] Tamura, T., Iizuka, R., et al. “An X-Ray Spectroscopic Search for Dark Matter in the Perseus Cluster with Suzaku.” *Publications of the Astronomical Society of Japan*, Vol. 67, No. 2, 2015, p. 23. https://doi.org/10.1093/pasj/psu156.

[14] Dark Matter. Wikipedia, Jun 20, 2022.

[15] Drees, M., and Gerbier, G. “Mini--Review of Dark Matter: 2012.” *arXiv e-prints*, 2012, p. arXiv:1204.2373.

[16] Bertone, G., and Merritt, D. “Dark Matter Dynamics and Indirect Detection.” *Modern Physics Letters A*, Vol. 20, No. 14, 2005, pp. 1021–1036. https://doi.org/10.1142/S0217732305017391.

[17] National Academies of Sciences, E. *Pathways to Discovery in Astronomy and Astrophysics for the 2020s*. 2021.

[18] Hartle, J. B. *Gravity: An Introduction to Einstein’s General Relativity*. Addison-Wesley, San Francisco, CA, 2003.

[19] Diemand, J., Kuhlen, M., et al. “Clumps and Streams in the Local Dark Matter Distribution.” *Nature*, Vol. 454, No. 7205, 2008, pp. 735–738. https://doi.org/10.1038/nature07153.

[20] Belbruno, E., and Green, J. “When Leaving the Solar System: Dark Matter Makes a Difference.” *Monthly Notices of the Royal Astronomical Society*, Vol. 510, No. 4, 2022, pp. 5154–5163. https://doi.org/10.1093/mnras/stab3781.

[21] Duncan, M., Quinn, T., et al. “The Formation and Extent of the Solar System Comet Cloud.” *The Astronomical Journal*, Vol. 94, 1987, p. 1330. https://doi.org/10.1086/114571.

[22] National Academies of Sciences, Engineering, and Medicine. *Origins, Worlds, and Life: A Decadal Strategy for Planetary Science and Astrobiology 2023-2032*. The National Academies Press, 2022.

[23] Johns Hopkins University Applied Physics Laboratory. Parker Solar Probe Becomes Fastest-Ever Spacecraft. *Parker Solar Probe*. http://parkersolarprobe.jhuapl.edu/News-Center/Show-Article.php?articleID=109. Accessed Sep. 8, 2019.

[24] Wertz, J. R., Everett, D. F., et al. *Space Mission Engineering: The New SMAD*. Microcosm Press, 2011.

[25] Landis, G. Microwave Pushed Interstellar Sail - Starwisp Revisited. 2000.

[26] Lubin, P., Hughes, G., et al. “Directed Energy for Relativistic Propulsion and Interstellar Communications.” *Journal of the British Interplanetary Society*, Vol. 68, No. 5/6, 2015, pp. 172–182.

[27] McNutt Jr., R. L., Paul, M. V., et al. *Interstellar Probe: Humanity’s Journal to Interstellar Space*. 2021.

[28] Lubin, P. “A Roadmap to Interstellar Flight.” *arXiv:1604.01356 [astro-ph, physics:physics]*, 2016.

[29] Manchester, Z., Peck, M., et al. “KickSat: A Crowd-Funded Mission to Demonstrate the World’s Smallest Spacecraft.” *AIAA/USU Conference on Small Satellites*, 2013, pp. SSC13-IX–5.

[30] Adams, V., and Peck, M. “R-Selected Spacecraft.” 2019. https://doi.org/10.31224/osf.io/wxhpt.

[31] Bible, J. J., Johansson, I., et al. Relativistic Propulsion Using Directed Energy. No. 8876, 2013, pp. 887605.

[32] Thornton, C. L., and Border, J. S. *Radiometric Tracking Techniques for Deep Space Navigation*. John Wiley & Sons, Inc., Hoboken, New Jersey, 2003.

[33] Bhaskaran, S. Autonomous Navigation for Deep Space Missions. Stockholm, Sweden, 2012.

[34] Riedel, J., Bhaskaran, S., et al. *Autonomous Optical Navigation (AutoNav)*. 2004, p. 138.

[35] Winternitz, L. M. B., Mitchell, J. W., et al. SEXTANT X-Ray Pulsar Navigation Demonstration: Flight System and Test Results. 2016.

[36] Winternitz, L. B., Hassouneh, M. A., et al. SEXTANT X-Ray Pulsar Navigation Demonstration: Additional On-Orbit Results. Marseille, France, 2018.

[37] Rivera, K. R. D., and Peck, M. A. The Application of Saturn’s Rings to Spacecraft Optical Navigation. In *AIAA SCITECH 2022 Forum*, American Institute of Aeronautics and Astronautics.

[38] Heintz, A., and Peck, M. A. Autonomous Optical Navigation for Resident Space Object Exploration. In *AIAA Scitech 2020 Forum*, American Institute of Aeronautics and Astronautics.

[39] Rivera, K. R. D., and Peck, M. A. Autonomous Navigation Using Novel Sources at Jupiter. In *AIAA Scitech 2020 Forum*, American Institute of Aeronautics and Astronautics.

[40] Lightsey, G. E., and Christian, J. A. "Onboard Image-Processing Algorithm for a Spacecraft Optical Navigation Sensor System." *Journal of Spacecraft and Rockets*, Vol. 49, No. 2, 2012, pp. 337–352. https://doi.org/10.2514/1.A32065.

[41] Adams, V. H., and Peck, M. A. Lost in Space and Time. Grapevine, Texas, 2017.

[42] Franklin, R. G., and Birx, D. L. "A Study of Natural Electromagnetic Phenomena for Space Navigation." *Proceedings of the IRE*, Vol. 48, No. 4, 1960, pp. 532–541. https://doi.org/10.1109/JRPROC.1960.287403.

[43] Chen, X., Sun, Z., et al. "A Novel Autonomous Celestial Integrated Navigation for Deep Space Exploration Based on Angle and Stellar Spectra Shift Velocity Measurement." *Sensors*, Vol. 19, No. 11, 2019, p. 2555. https://doi.org/10.3390/s19112555.

[44] Santerre, R., Geiger, A., et al. "Geometry of GPS Dilution of Precision: Revisited." *GPS Solutions*, Vol. 21, No. 4, 2017, pp. 1747–1763. https://doi.org/10.1007%2Fs10291-017-0649-y.

[45] European Space Agency. Gaia Mission Science Performance - Gaia - Cosmos. https://www.cosmos.esa.int/web/gaia/science-performance. Accessed May 17, 2022.

[46] Dornier Satellitensysteme GmbH. "LISA Final Technical Report." 2000, p. 504.

[47] Faraoni, V. *Special Relativity*. Springer Science & Business Media, 2013.

[48] Draine, B. T. *Physics of the Interstellar and Intergalactic Medium*. Princeton University Press, Princeton, New Jersey, 2011.

[49] Einstein, A. "Zur Elektrodynamik Bewegter Körper." *Annalen der Physik*, Vol. 322, No. 10, 1905, pp. 891–921. https://doi.org/10.1002/andp.19053221004.

[50] Einstein, A. “Die Grundlage Der Allgemeinen Relativitätstheorie.” *Annalen der Physik*, Vol. 354, No. 7, 1916, pp. 769–822. https://doi.org/10.1002/andp.19163540702.

[51] Oliver, B. M. “The View from the Starship Bridge and Other Observations.” *IEEE Spectrum*, Vol. 1, No. 1, 1964, pp. 86–92. https://doi.org/10.1109/MSPEC.1964.5531934.

[52] Klioner, S. “General Relativistic Model of VLBI Observables.” *Proceedings of AGU Chapman Conference on Geodetic VLBI: Monitoring Global Change*, 1991.

[53] Turyshev, S. G. Relativistic Navigation: A Theoretical Foundation. http://arxiv.org/abs/gr-qc/9606063. Accessed Jul. 6, 2022.

[54] Yucalan, D., and Peck, M. A Static Estimation Method for Autonomous Navigation of Relativistic Spacecraft. 2019.

[55] Klioner, S. A., and Kopeikin, S. M. “Microarcsecond Astrometry in Space - Relativistic Effects and Reduction of Observations.” *The Astronomical Journal*, Vol. 104, 1992, p. 897. https://doi.org/10.1086/116284.

[56] Felice, F. de, Preti, G., et al. “Relativistic Satellite Astrometry: The Stellar Radial Velocity.” *Astronomy & Astrophysics*, Vol. 528, 2011, p. A23. https://doi.org/10.1051/0004-6361/201015375.

[57] Schuh, H., and Behrend, D. “VLBI: A Fascinating Technique for Geodesy and Astrometry.” *Journal of Geodynamics*, Vol. 61, 2012, pp. 68–80. https://doi.org/10.1016/j.jog.2012.07.007.

[58] Hees, A., Bertone, S., et al. “Relativistic Formulation of Coordinate Light Time, Doppler, and Astrometric Observables up to the Second Post-Minkowskian Order.” *Physical Review D*, Vol. 89, No. 6, 2014, p. 064045. https://doi.org/10.1103/PhysRevD.89.064045.

[59] Titov, O., and Girdiuk, A. “Applying the Theory of General Relativity to Reducing Geodetic VLBI Data.” *Astronomy & Astrophysics*, Vol. 574, 2015, p. A128. https://doi.org/10.1051/0004-6361/201424690.

[60] Hoag, D. G., and Wrigley, W. “Navigation and Guidance in Interstellar Space.” *Acta Astronautica*, Vol. 2, No. 5, 1975, pp. 513–533. https://doi.org/10.1016/0094-5765(75)90065-X.

[61] Semyonov, O. G. “Kinematics of Maneuverable Relativistic Starship.” *Acta Astronautica*, Vol. 75, 2012, pp. 85–94. https://doi.org/10.1016/j.actaastro.2012.01.012.

[62] Calabro, E. “Relativistic Aberrational Interstellar Navigation.” *Acta Astronautica*, Vol. 69, No. 7, 2011, pp. 360–364. https://doi.org/10.1016/j.actaastro.2011.05.013.

[63] Bitetto, D. M. A. V. *A RELATIVISTIC NAVIGATION BASED SYSTEM*. Dr. Marco A. V. Bitetto, 2011.

[64] Tartaglia, A. Relativistic Space-Time Positioning: Principles and Strategies. http://arxiv.org/abs/1212.0429. Accessed Jul. 6, 2022.

[65] Yucalan, D., and Peck, M. “Autonomous Navigation of Relativistic Spacecraft in Interstellar Space.” *Journal of Guidance, Control, and Dynamics*, 2021, pp. 1–10. https://doi.org/10.2514/1.G005340.

[66] Zhu, J.-P., Zhang, B., et al. “Relativistic Astronomy. II. In-Flight Solution of Motion and Test of Special Relativity Light Aberration.” *The Astrophysical Journal*, Vol. 877, No. 1, 2019, p. 14. https://doi.org/10.3847/1538-4357/ab1650.

[67] Christian, J. A. “StarNAV: Autonomous Optical Navigation of a Spacecraft by the Relativistic Perturbation of Starlight.” *Sensors*, Vol. 19, No. 19, 2019, p. 4064. https://doi.org/10.3390/s19194064.

[68] Yucalan, D., and Peck, M. A. An Optimal Navigation Filter for Relativistic Spacecraft. Virtual Event, 2021.

[69] Bailer-Jones, C. A. L. “Lost in Space? Relativistic Interstellar Navigation Using an Astrometric Star Catalog.” *Publications of the Astronomical Society of the Pacific*, Vol. 133, No. 1025, 2021, p. 074502. https://doi.org/10.1088/1538-3873/ac0774.

[70] Parkinson, B. W., and Spilker, J. J. *Global Positioning System: Theory and Applications*. AIAA, 1996.

[71] Bahder, T. B. “Navigation in Curved Space–Time.” *American Journal of Physics*, Vol. 69, No. 3, 2001, pp. 315–321. https://doi.org/10.1119/1.1326078.

[72] Sheikh, S. I., Pines, D. J., et al. “Spacecraft Navigation Using X-Ray Pulsars.” *Journal of Guidance, Control, and Dynamics*, Vol. 29, No. 1, 2006, pp. 49–63. https://doi.org/10.2514/1.13331.

[73] Denisov, M. M. “Relativistic Corrections in the Laser Ranging of Spacecrafts.” *Mathematical Models and Computer Simulations*, Vol. 1, No. 3, 2009, pp. 393–401. https://doi.org/10.1134/S2070048209030065.

[74] Hećimović, Ž. “Relativistic Effects on Satellite Navigation.” *Tehnički vjesnik/Technical Gazette, http://hrcak.srce.hr/index.php?show=clanak&id_clanak_jezik=143530*, Vol. 20, 2013, pp. 195–203.

[75] Carroll, S. M. *Spacetime and Geometry, An Introduction to General Relativity*. Addison-Wesley, San Fransisco, CA, 2004.

[76] Einstein, A. On the Relativity Principle and Conclusions Drawn from It. In *Jahrbuch der Radioaktivitaet und Elektronik*, 1907, pp. 411–462.

[77] Brecher, K. “Is the Speed of Light Independent of the Velocity of the Source.” *Physical Review Letters*, Vol. 39, 1977, pp. 1051–1054. https://doi.org/10.1103/PhysRevLett.39.1051.

[78] United States Naval Observatory. International Celestial Reference System (ICRS). .

[79] Einstein, A. How I Created the Theory of Relativity. Physics Today, Aug, 1982.

[80] Ben-Israel, A., and Greville, T. N. E. *Generalized Inverses: Theory and Applications*. Springer-Verlag, New York, 2003.

[81] Breakthrough Starshot. *Breakthrough Initiatives*. https://breakthroughinitiatives.org/initiative/3. Accessed Aug. 13, 2019.

[82] NASA Goddard Space Flight Center. High Energy Astrophysics Science Archive Research Center (HEASARC) Browse: List of Star-Catalog Catalogs. Apr 22, 1998.

[83] European Space Agency Gaia Collaboration. “Gaia Data Release 2. Summary of the Contents and Survey Properties.” *Astronomy and Astrophysics*, Vol. 616, 2018, p. A1. https://doi.org/10.1051/0004-6361/201833051.

[84] TheNauticalAlmanac.com. 2019 Nautical Almanac. .

[85] European Space Agency (ESA), and Gaia Data Processing and Analysis Consortium (DPAC). Gaia Data Release 2 Documentation Release 1.2. Jun 05, 2019.

[86] European Southern Observatory. European Southern Observatory (ESO) - The Very Large Telescope Interferometer (VLTI). May 24, 2000.

[87] McKee, P., Kowalski, J., et al. “Navigation and Star Identification for an Interstellar Mission.” *Acta Astronautica*, Vol. 192, 2022, pp. 390–401. https://doi.org/10.1016/j.actaastro.2021.12.007.

[88] Rumble, J. R. *Handbook of Chemistry and Physics*. CRC Press.

[89] Zarchan, P., and Musoff, H. *Fundamentals of Kalman Filtering: A Practical Approach*. American Institute of Aeronautics and Astronautics, 2009.

[90] European Space Agency (ESA), and Gaia Data Processing and Analysis Consortium (DPAC). Gaia Early Data Release 3 Documentation Release 1.1. Mar 03, 2021.

[91] de Salas, P. F., Malhan, K., et al. “On the Estimation of the Local Dark Matter Density Using the Rotation Curve of the Milky Way.” *Journal of Cosmology and Astroparticle Physics*, Vol. 2019, No. 10, 2019, pp. 037–037. https://doi.org/10.1088/1475-7516/2019/10/037.

[92] GRACE | Mission. *GRACE Tellus*. https://grace.jpl.nasa.gov/mission/grace. Accessed Jun. 6, 2022.

[93] Steitz, D. E., O’Donnell, F., et al. *GRACE Launch Press Kit*. 2002.

[94] Drinkwater, M., Haagmans, R., et al. *GOCE: Obtaining a Portrait of Earth’s Most Intimate Features*. 2008.

[95] ESA. GOCE (Gravity Field and Steady-State Ocean Circulation Explorer) Sensor Complement. https://directory.eoportal.org/web/eoportal/satellite-missions/g/goce#sensors.

[96] Zuber, M. T., Smith, D. E., et al. Gravity Recovery and Interior Laboratory (GRAIL) Mission: Status at the Initiation of the Science Mapping Phase. 2012.

[97] Flechtner, F., Morton, P., et al. Status of the GRACE Follow-On Mission.

[98] European Space Agency. GOCE Calibration. https://www.esa.int/Applications/Observing_the_Earth/FutureEO/GOCE/Calibration. Accessed Jul. 28, 2022.

[99] Voyager 1. Wikipedia, Jun 11, 2022.

[100] Sun. Wikipedia, May 29, 2022.

[101] Jupiter. Wikipedia, Jun 13, 2022.

[102] Bate, R. R., Mueller, D. D., et al. *Fundamentals of Astrodynamics*. Courier Corporation, 1971.

[103] Vallado, D. A. *Fundamentals of Astrodynamics and Applications*. Springer Science & Business Media, 2001.

[104] Sims, J. A. *Delta-V Gravity-Assist Trajectory Design: Theory and Practice*. Purdue University, 1996.

[105] Juno (Spacecraft). Wikipedia, Jun 15, 2022.

[106] Earth. Wikipedia, Jun 10, 2022.

[107] Raymond, S. N. Hill Radius/Sphere. Encyclopedia of Astrobiology, Springer, Dec 13, 2020.

[108] Kafle, P. R., Sharma, S., et al. "ON THE SHOULDERS OF GIANTS: PROPERTIES OF THE STELLAR HALO AND THE MILKY WAY MASS DISTRIBUTION." *The Astrophysical Journal*, Vol. 794, No. 1, 2014, p. 59. https://doi.org/10.1088/0004-637X/794/1/59.

[109] Milky Way. Wikipedia, Jun 21, 2022.

[110] Bruijne, J. H. J. de, Allen, M., et al. "Detecting Stars, Galaxies, and Asteroids with Gaia." *Astronomy & Astrophysics*, Vol. 576, 2015, p. A74. https://doi.org/10.1051/0004-6361/201424018.

[111] Gaia. Gaia Spacecraft Overview – Gaia. https://spaceflight101.com/gaia/gaia-spacecraft-overview/. Accessed Jun. 15, 2022.

[112] Jet Propulsion Laboratory. Voyager - The Spacecraft. https://voyager.jpl.nasa.gov/mission/spacecraft/. Accessed Jun. 14, 2022.

[113] Liebe, C. C. "Star Trackers for Attitude Determination." *IEEE AES Systems Magazine*, 1995.

[114] Sechi, G., Buonocore, M., et al. "In-Flight Results from the Drag-Free and Attitude Control of GOCE Satellite." *IFAC Proceedings Volumes*, Vol. 44, No. 1, 2011, pp. 733–740. https://doi.org/10.3182/20110828-6-IT-1002.02966.

[115] Marie, J., Cordero, F., et al. In-Orbit Experience of the Gaia and LISA Pathfinder Cold Gas Micro-Propulsion Systems. Marseille, France, 2018.

[116] Goddard Spaceflight Center. *Rules for the Design, Development, and Operation of Flight Systems*. 2021.

[117] Jet Propulsion Laboratory. New Horizons: Systems and Components. http://pluto.jhuapl.edu/Mission/Spacecraft/Systems-and-Components.php.

[118] Caldwell, S. 3.0 Power. *NASA*. http://www.nasa.gov/smallsat-institute/sst-soa/power. Accessed Jun. 17, 2022.

[119] Put, P. L., List, M., et al. “Development of an Advanced Proportional Xenon Feed Assembly for the GOCE Spacecraft.” 2004.

[120] Gaia. ESA Science & Technology - Spacecraft. https://sci.esa.int/web/gaia/-/40128-overview. Accessed Jun. 15, 2022.

[121] Garcia-Garcia, Q., Allica, J., et al. GAIA Satellite Phase Array Antenna. 2010.

[122] Ludwig, R., and Taylor, J. Voyager Telecommunications. In *Deep Space Communications*, John Wiley & Sons, Ltd, 2016, pp. 37–77.

[123] Nguyen, H., Köhler, J., et al. “The Merits of Cold Gas Micropropulsion in State-of-the-Art Space Missions.” 2002.

[124] Sgobba, T., and Rongier, I. *Space Safety Is No Accident: The 7th IAASS Conference*. Springer, 2015.

[125] Perryman, M. a. C. “GAIA: An Introduction to the Project.” *EAS Publications Series*, Vol. 2, 2002, pp. 3–26. https://doi.org/10.1051/eas:2002001.

[126] SpaceX. *Starship Payload Guide*. 2020.

[127] Akin, D. L. Mass Estimating Relations. University of Maryland, , 2016.

[128] Nancy Grace Roman Space Telescope. Wikipedia, Apr 05, 2022.

[129] European Space Agency. GOCE - Facts and Figures. https://www.esa.int/Applications/Observing_the_Earth/FutureEO/GOCE/Facts_and_figures. Accessed Jun. 21, 2022.

[130] European Space Agency. Frequently Asked Questions about Gaia. https://www.esa.int/Science_Exploration/Space_Science/Gaia/Frequently_Asked_Questions_about_Gaia. Accessed Jun. 21, 2022.

[131] Jet Propulsion Laboratory. Voyager - Fact Sheet. https://voyager.jpl.nasa.gov/frequently-asked-questions/fact-sheet/. Accessed Jun. 21, 2022.

[132] SpaceX Starship. Wikipedia, Jun 21, 2022.

[133] Rokot. Wikipedia, May 04, 2022.

[134] Soyuz-2. Wikipedia, Jun 11, 2022.

[135] Titan IIIE. http://www.astronautix.com/t/titaniiie.html. Accessed Jun. 21, 2022.